communications biology

A Nature Portfolio journal

Article

https://doi.org/10.1038/s42003-025-07717-5

Induction of MASH-like pathogenesis in the *Nwd1*$^{-/-}$ mouse liver

Seiya Yamada[1,2] ✉, Hayato Ogawa[1], Miona Funato[1], Misaki Kato[1], Kazuhiko Nakadate[3], Tomoya Mizukoshi[1], Kiyoharu Kawakami[3], Ryosuke Kobayashi[4], Takuro Horii[4], Izuho Hatada[4,5] & Shin-ichi Sakakibara[1] ✉

Endoplasmic reticulum (ER) stores Ca^{2+} and plays crucial roles in protein folding, lipid transfer, and it's perturbations trigger an ER stress. In the liver, chronic ER stress is involved in the pathogenesis of metabolic dysfunction-associated steatotic liver disease (MASLD) and metabolic dysfunction-associated steatohepatitis (MASH). Dysfunction of sarco/endoplasmic reticulum calcium ATPase (SERCA2), a key regulator of Ca^{2+} transport from the cytosol to ER, is associated with the induction of ER stress and lipid droplet formation. We previously identified NACHT and WD repeat domain-containing protein 1 (Nwd1) localized at the ER and mitochondria. However, the physiological significance of Nwd1 outside the brain remains unclear. In this study, we revealed that *Nwd1*$^{-/-}$ mice exhibited pathological manifestations comparable to MASH. Nwd1 interacts with SERCA2 near ER membranes. *Nwd1*$^{-/-}$ livers exhibited reduced SERCA2 ATPase activity and a smaller Ca^{2+} pool in the ER, leading to an exacerbated state of ER stress. These findings highlight the importance of SERCA2 activity mediated by Nwd1 in the pathogenesis of MASH.

Metabolic dysfunction-associated steatotic liver disease (MASLD, previously called non-alcoholic fatty liver disease, NAFLD) and metabolic dysfunction-associated steatohepatitis (MASH, previously called non-alcoholic steatohepatitis, NASH) are liver diseases that progress without symptoms, and they are linked to global public health problems[1]. Characterized by the accumulation of lipid droplets in the liver, MASH evolves from steatosis to inflammation and cellular damage, including cell death, often culminating in fibrosis, cirrhosis, and eventually hepatocellular carcinoma[2]. The etiology of hepatic lipid accumulation involves various factors, including the excessive uptake or synthesis of fatty acids, defective transport of very low-density lipoprotein (VLDL), and impaired beta-oxidation of fatty acids[3,4]. Furthermore, spatially controlled hepatic zonation is crucial for physiological liver function, encompassing the metabolism of various endogenous products and xenobiotics[5–7]. A comprehensive understanding of the intricate interplay of cellular processes in MASH pathogenesis is imperative for developing targeted therapeutic interventions. Although several clinical trials of pharmacotherapies for MASH treatment are ongoing[2], no effective treatment has been developed.

MASLD and MASH are considered polygenic disorders entailing a diverse array of genes, including unidentified genes. However, the individual contributions of these genes to the pathogenesis of these diseases are unclear. One crucial aspect of MASH pathology is the dysregulation of endoplasmic reticulum (ER) homeostasis[8,9]. The ER stores Ca^{2+} and plays crucial roles in protein folding, lipid transfer, and organelle dynamics regulation. The accumulation of unfolded or misfolded proteins in the ER activates a series of homeostatic responses collectively termed ER stress, and chronic ER stress contributes to the pathogenesis of MASLD and MASH, including liver steatosis and lipid droplet formation[10,11]. The ER-localized transmembrane protein BSCL2/SEIPIN, acting at ER–lipid droplet contact sites, facilitates the incorporation of protein and lipid cargo into growing lipid droplets and helps connect newly formed lipid droplets to the ER and stabilize ER–lipid droplet contacts[12]. Recent studies suggested that the abnormal regulation of Ca^{2+} transport proteins is the basis of MASLD/MASH[13,14]. The expression of type II inositol 1,4,5-trisphosphate receptor, the principal Ca^{2+}-release channel in hepatocytes, was dramatically decreased in biopsied livers from patients with steatosis and MASH[15]. Consistently, dysfunction of sarco/endoplasmic reticulum calcium ATPase (SERCA2), a key regulator of Ca^{2+} transport from the cytosol to the ER, induces ER stress and lipid droplet formation[16]. Conversely, SERCA2 overexpression in obese mice reduced lipid synthesis gene expression and triglyceride content, emphasizing its significance in dysregulated lipid homeostasis and suggesting that SERCA2

[1]Laboratory for Molecular Neurobiology, Faculty of Human Sciences, Waseda University, Tokorozawa, Saitama, Japan. [2]Neuroscience Center, HiLIFE—Helsinki Institute of Life Science, University of Helsinki, Helsinki, Finland. [3]Department of Functional Morphology, Meiji Pharmaceutical University, Kiyose, Tokyo, Japan. [4]Laboratory of Genome Science, Biosignal Genome Resource Center, Institute for Molecular and Cellular Regulation, Gunma University, Maebashi, Gunma, Japan. [5]Viral Vector Core, Gunma University Initiative for Advanced Research (GIAR), Gunma, Japan. ✉e-mail: seiya.s.yamada@gmail.com; sakakiba@waseda.jp

could be targeted to treat MASH[17]. However, the molecular mechanism by which SERCA2 acquires its proper function in ER remains unclear.

Our prior research identified the NACHT and WD repeat domain-containing protein 1 (Nwd1) gene, a member of the signal transduction ATPases with numerous domains (STAND) protein superfamily[18,19]. Nwd1 is localized at the ER and mitochondria in neural stem/progenitor cells (NSPCs), and it is essential for normal brain development via interactions with the purine-synthesizing enzyme PAICS to regulate purinosome assembly in NSPCs[18,19]. Nwd1 is a multi-domain protein; i.e., it has a NACHT domain in the central region that is predicted to have nucleoside triphosphatase activity, an effector domain at the N-terminus that binds to PAICS, and a cluster of WD40 repeats at the C-terminus that is involved in interactions with other proteins or ligands. Based on its domain structure, Nwd1 is classified into the STAND superfamily, which is known to be involved in the formation of large protein complexes required for various signaling cascades such as apoptosis (apoptosome) and inflammation (inflammasome) and is conserved across species, including zebrafish, mice, rats, monkeys, and humans[18,20,21]. We previously demonstrated that Nwd1 is predominantly expressed in the liver in addition to the brain[18,20,21]; however, the physiological role of Nwd1 in nonneural tissues remains unknown.

In this study, we revealed that the livers of *Nwd1*$^{-/-}$ mice exhibit pathological manifestations resembling MASH, implying that *Nwd1* plays a role in modulating liver homeostasis by regulating the Ca^{2+} pump function of SERCA2. These findings could provide clues to understanding the pathogenesis of ER stress-induced MASH.

Methods

Generation of Nwd1 knockout mice

All protocols were approved by the committees on the ethics of animal experiments at Gunma University and Waseda University. We have complied with all relevant ethical regulations for animal use. C57BL/6J mice purchased from Japan SLC, Inc. (Shizuoka, Japan) were housed under temperature- and humidity-controlled conditions on a 12-h/12-h light/dark cycle with *ad libitum* access to normal food and water. The day of birth was designated as P0. *Nwd1*^{flox} mice were generated via electroporation, as previously reported with a partial modification[22]. Corresponding to the target DNA sequences (Nwd1L3, AATGGGACAGTCACTTGGGA; Nwd1R1, ACAGAACCTGGATTTTGTGG), donor single-stranded oligodeoxynucleotides (ssODNs) with 5′- and 3′-homology arms flanking loxP and a restriction site were designed (Nwd1L3loxpAS, cacacacacaTGCATGTGCTCACACATCCTAACCTGCCATGTGGGCTTTTGC AAGCCATCATAACTTCGTATAATGTATGCTATACGAAGTTATGG ATCCCCAAGTGACTGTCCCATTTGTTAAACTTCACAGTCTGTGT CCCTCCGAACATGTTTCCCA; Nwd1R1loxP, GCCACATGCATGCT GCTTCCTTCCTTTTTTGTAGGGATTTGGACAGAACCTGGATTTT GTATAACTTCGTATAATGTATGCTATACGAAGTTATAAGCTTGG AGGTTAGTTATGTGTTGTGTGATTGAGCCTGGGCCCCAGACCtgc atgtagcctttgt; Fig. 1A). Pre-annealed crRNA (Alt-R CRISPR–Cas9 crRNA, Integrated DNA Technologies [IDT], Coralville, IA, USA])/tracrRNA (Alt-R CRISPR–Cas9 tracrRNA, IDT; 3 μM), recombinant Cas9 protein (100 ng/μl; GeneArt Platinum Cas9 Nuclease, Thermo Fisher Scientific, Waltham, MA, USA), and ssODNs (400 ng/μl; Ultramer, IDT) in Opti-MEM I (Thermo Fisher Scientific) were used for electroporation. First, a left loxP site was introduced into intron 4 of *Nwd1* by electroporation using B6D2F1-derived zygotes, and then the edited embryos were transferred to the oviduct of pseudopregnant ICR female to obtain *Nwd1* left loxPed males. Next, *Nwd1*^{flox} mice were generated by introducing a right loxP site into intron 5 of *Nwd1* using left loxPed male-derived zygotes. Floxed alleles were confirmed by sequencing PCR products using the following primer set: 5′-CAGGTGTGATATGTAAATACTTCTTTG-3′ (F2) and 5′-CAGGCC-TAACAGAGCCAGAC-3′ (R2). We further converted the floxed allele to a null allele (*Nwd1*$^{-}$) by crossing *Nwd1*^{flox} heterozygous mice with CAG-Cre driver mice (B6.Cg-Tg[CAG-Cre]CZ-MO2Osb, RBRC01828; RIKEN BRC, Tokyo, Japan) harboring the CAG-promoter-driven Cre recombinase transgene[23]. Exon 5, which encodes the NACHT domain, was eliminated by Cre/loxP-mediated excision. The genotyping of floxed and null alleles was performed by genomic PCR using the following primer sets: 5′-TCAC ACATCCTAACCTGCCA-3′ (F1) and 5′-AGTAGGCCAAGCTCGATC TC-3′ (R1) for the floxed allele and F1 and R2 primers for the null allele. For immunostaining, electron microscopy, and general histological analysis, *Nwd1*$^{-/-}$ and the littermate male mice aged 2–7 months were used unless otherwise noted.

Cell culture and transfection

HEK293 (JCRB9068, Japanese Collection of Research Bioresources Cell Bank, Osaka, Japan) and HeLa (RCB0007, RIKEN Cell Bank, Tsukuba, Japan) cells were cultured in Dulbecco's Modified Eagle Medium (DMEM, FUJIFILM Wako, Osaka, Japan) containing 10% fetal bovine serum (FBS) (Biowest, Nuaillé, France), 1% penicillin/streptomycin (FUJIFILM Wako Pure Chemical), and 1% L-glutamine (FUJIFILM Wako). Mouse hepatocyte cell line AML12 (alpha mouse liver 12) was purchased from ATCC (American Type Culture Collection, cat number CRL-2254) and cultured in DMEM/Ham's F-12 (FUJIFILM Wako) containing 10% FBS, and 1% Insulin-Transferrin-Selenium supplement (ITS-G, FUJIFILM Wako), and 40 ng/mL dexamethasone (FUJIFILM Wako). Cells were seeded into poly-D-lysine–coated dishes (Merck Millipore, Burlington, MA, USA) and transfected with plasmid DNA and PEI MAX (Polysciences, Warrington, PA, USA) complexes (DNA to PEI MAX ratio, 1:3, w/w) formed in Opti-MEM (Thermo Fisher Scientific) via incubation for 15 min at 25°C. DNA complexes were added to cell cultures with Opti-MEM for 3 h, followed by cultivation with serum-containing DMEM or DMEM/F-12.

Electron microscopy

Anesthetized adult were perfused transcardially with saline solution, followed by a fixative containing 2% paraformaldehyde (PFA) and 2% glutaraldehyde (GA) in 0.1 M phosphate buffer (PB), pH 7.4. Liver tissue was dissected, cut into small pieces, washed several times with PB, and postfixed with 1% OsO_4 (TAAB Laboratories, Aldermaston, UK) for 2 h. After dehydration with ethanol and replacement with propylene oxide, the sections were embedded in Epon-812 resin (TAAB Laboratories) and thermally polymerized. After trimming, the samples were cut into 70-nm-thick sections, electron-stained with uranium and lead, and observed and photographed using a transmission electron microscope (HT7800, Hitachi, Tokyo, Japan). For immunoelectron microscopy, HeLa cells expressing Flag-Nwd1 grown on glass coverslips were fixed with 4% PFA and 0.05% GA in 0.1 M PB (pH 7.4). The cells were washed with PB and treated with 30% sucrose in 0.1 M PB, and rapid freeze fractionation was performed using liquid nitrogen. Cells were blocked with normal goat serum for 2 h and incubated with anti-DDDDK-tag antibody for 2 h. After incubation with 1.4-nm gold-conjugated secondary antibody (Nanoprobes, Yaphank, NY, USA) for 1 h, the signals were gold-sensitized using a gold-enhancing kit (Nanoprobes). After washing with H_2O, cells were refixed with 1% OsO_4 for 1 h, treated with ethanol and propylene oxide, and embedded in Epon-812 resin. Sections (70 nm thick) were electron-stained with uranium and lead and photographed using a transmission electron microscope (HT7800).

Plasmids

pCAG-EGFP-Nwd1 was cloned in the previous study[19]. pN3-3 × Flag-Control was purchased from Addgene (Watertown, MA, USA, plasmid #107717, deposited by Dr. Suske)[24]. To construct 3×Flag-Nwd1 (hereafter called Flag-Nwd1), the full-length *Nwd1* cDNA was isolated using RT-PCR of total RNA from E12 embryonic and adult mice brains and then subcloned in-frame into the pN3-3 × Flag-Control plasmid. *Nwd1* cDNA corresponding to the N-terminal or C-terminal region of the protein (accession number BC082552; 4–1026 bp for the N-terminus and 2578–4563 bp for the C-terminus) was subcloned into C-Flag-pcDNA3 (Addgene, plasmid # 20011, deposited by Dr. Smale)[25] and pN3-3×Flag-Control to construct Flag-Nwd1-N and 3 × Flag-Nwd1-C (hereafter called Flag-Nwd1-C). To construct Halo-Nwd1, full-length Nwd1 cDNA was subcloned into the pFN21A-HaloTag-CMV Flexi-vector (Promega, Madison, WI, USA). To

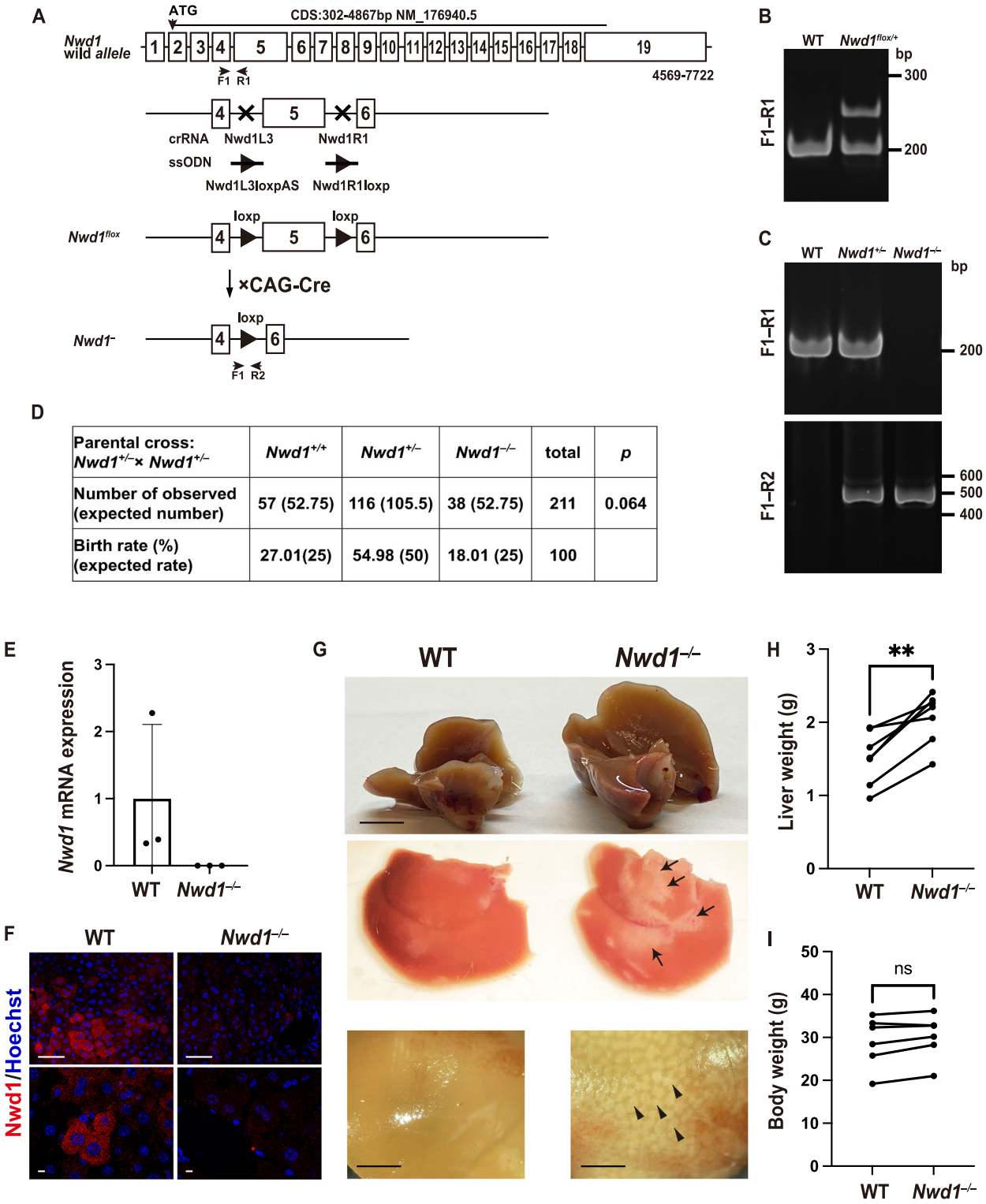

Parental cross: *Nwd1*$^{+/-}$× *Nwd1*$^{+/-}$	*Nwd1*$^{+/+}$	*Nwd1*$^{+/-}$	*Nwd1*$^{-/-}$	total	*p*
Number of observed (expected number)	57 (52.75)	116 (105.5)	38 (52.75)	211	0.064
Birth rate (%) (expected rate)	27.01(25)	54.98 (50)	18.01 (25)	100	

construct 3×Flag-SERCA2 (hereafter called Flag-SERCA2), the coding region of SERCA2b (Addgene, plasmid #75188, deposited by Dr. Lytton)[26] was subcloned in-frame into a pN3-3 × Flag-Control vector. The deletion mutants 3×Flag-SERCA2-N (amino acids 1–787, hereafter called Flag-Flag-SERCA2-N) and 3×Flag-SERCA2-C (amino acids 788–1044, hereafter called Flag-SERCA2-C) were constructed from 3 × Flag-SERCA2 using a Q5 Site-Directed Mutagenesis Kit (New England BioLabs, Ipswich, MA, USA). mCherry-Sec61B (Addgene, plasmid # 121160, deposited by Dr. Mayr)[27] was used for ER imaging.

Primary antibodies

The following primary antibodies were used: anti-Nwd1 (rabbit polyclonal[19]; 1:400 for immunocytochemistry [ICC]), anti-cleaved caspase-3 (Asp175) (rabbit polyclonal, #9661, RRID: AB_2341188, Cell Signaling Technology, Danvers, MA, USA; 1:400 for immunohistochemistry [IHC]), anti-cleaved caspase-1 (Ala317) p10 (rabbit polyclonal, #AF4022, RRID: AB_2845464, anti-F4/80 (rabbit polyclonal, #28463-1-AP, RRID: AB_2881149, Proteintech, Rosemont, IL, USA; 1:800 for IHC), Affinity Biosciences, Cincinnati, OH, USA; 1:200 for IHC), anti-BSCL2/SEIPIN

Fig. 1 | Generation of *Nwd1* knockout mice. A Schematic diagram of the Nwd1 wild-type allele (top) and the conditional allele of Nwd1flox (middle), in which LoxP sequences were inserted into the introns on both sides (crRNA targeting sites: Nwd1L3 and Nwd1R1) of exon 5 *via* two rounds of genomic editing using ssODNs (Nwd1L3loxpAS and Nwd1R1loxP). $Nwd1^{flox}$ mice were crossed with CAG-Cre transgenic mice harboring CAG promoter-driven Cre recombinase to generate the $Nwd1^{-}$ null allele (bottom). Upon elimination of the floxed *Nwd1* critical exon (exon 5), this allele generates a truncated RNA lacking the NACHT domain of the open-reading frame of *Nwd1*. **B** PCR genotyping of wild-type or $Nwd1^{flox/+}$ tail genomic DNA. The specific primers (primer pair F1–R1 depicted in A) were used to detect wild-type (189-bp amplicon) and $Nwd1^{flox}$ (229-bp amplicon) alleles. PCR products were separated by 5% SDS-PAGE. **C** PCR genotyping of wild-type, $Nwd1^{+/-}$, and $Nwd1^{-/-}$ mice. Specific primers (primer pairs F1–R1 and F2–R2 depicted in **A**) were used to detect wild-type (189-bp amplicon) and $Nwd1^{-}$ (431-bp amplicon) alleles. PCR products were separated by 5% SDS-PAGE. **D** The table presents the genotypes and birth rates observed in 211 adult mice born from crosses between $Nwd1^{+/-}$ males and females. Numbers in parentheses represent the expected number of offspring and birth rate according to the Mendelian ratio. **E** Loss of *Nwd1* mRNA expression in $Nwd1^{-/-}$ livers. The mRNA isolated from wild-type ($n = 3$) and $Nwd1^{-/-}$ ($n = 3$) adult livers were subjected to qRT–PCR targeting for exon 5, and *Nwd1* expression was normalized to that of *β-actin* mRNA. The graph shows the mean ± SD. **F** Immunostaining of 10–12 month-old male liver tissues with antibody to Nwd1 (red). Nuclei were counterstained with Hoechst dye (blue). Lower panels are magnified views showing individual hepatocytes. **G** Gross anatomical observation of the 7-month-old male liver. $Nwd1^{-/-}$ livers exhibited hepatomegaly (upper), fiber-like structures on the surface (middle, arrows), and numerous abnormal hepatic lobules that turned whitish (lower, arrowheads). Liver ($n = 7$) (**H**) and body weight ($n = 6$) (**I**) of 2–9-month-old male $Nwd1^{-/-}$ mice and their wild-type littermates were compared by a paired *t*-test. Individuals connected by solid lines represent siblings. ns, not significant; **, $P < 0.01$. Black dots represent each independent biological replicate. Scale bars, 200 μm (F, upper), 5 μm (F, lower), 5 mm (G, upper) or 2 mm (G, lower).

(rabbit polyclonal, #ab106793, RRID: AB_10974250, Abcam, Cambridge, UK; 1:200 for IHC, 1:1000 for western blotting [WB]), anti-KDEL (mouse monoclonal, #M181-3, RRID: AB_10693914, MBL, Woburn, MA, USA; 1:400 for IHC, 1:400 for ICC, 1:5000 for WB), anti-LAMP1 (1D4B) (rat monoclonal, #sc-19992, RRID: AB_2134495, Santa Cruz Biotechnology, Dallas, TX, USA; 1:1000 for WB), anti-LC3A/B (D3U4C) XP (rabbit monoclonal, #12741, RRID: AB_2617131, Cell Signaling Technology; 1:200 for IHC, 1:2000 for WB), anti-SERCA2 ATPase Clone IID8 (mouse monoclonal, #NB300-529, RRID: AB_531361, Novus Biologicals, Centennial, CO, USA; 1:200 for ICC, 1:2500 for WB), anti-DDDDK-tag (mouse monoclonal, #M185-3, RRID: AB_11126775, MBL; 1:10000 for WB, 1:10000 for ICC), anti-ADP/ATP translocase 1/2 (ANT1/2, rabbit polyclonal, #17796-1-AP, RRID: AB_2190358, Proteintech; 1:2000 for WB), anti-voltage-dependent anion-selective channel protein 1 (VDAC1)/porin (mouse monoclonal, #ab14734, RRID: AB_443084, Abcam; 1:2000 for WB), anti-α-tubulin (rabbit polyclonal, #11224-1-AP, RRID: AB_2210206, Proteintech; 1:5000 for WB), anti-RAB5A (rabbit polyclonal, #11947-1-AP, RRID: AB_2269388, Proteintech; 1:2000 for WB), and anti-RAB7A (rabbit polyclonal, #55469-1-AP, RRID: AB_11182831, Proteintech; 1:2000 for WB).

Hematological and biochemical analysis of blood and plasma samples

Peripheral whole blood from 5 to 9 month-old male and female mice was collected and briefly mixed in Insepak II (Sekisui, Tokyo, Japan), followed by incubation at room temperature for 15–30 min. Subsequently, the mixture was centrifuged at 3500 rpm for 15 min, and the supernatant was collected as the plasma. Peripheral blood was collected using MiniCollect K2E K2EDTA tubes (Greiner Bio-One, Kremsmünster, Austria). Hematological and biochemical analyses were conducted by the BioSafety Research Center Inc. (Shizuoka, Japan).

Oil red O staining, Sirius red staining, periodic acid-Schiff (PAS) staining, and Congo red staining

General staining of liver tissue sections was performed using an Oil Red O Stain Kit (for fat staining) (ScyTek Laboratories, Logan, UT, USA), Picro-Sirius Red Stain Kit (for collagen staining) (ScyTek Laboratories), Periodic Acid-Schiff (PAS) Diastase Stain Kit (for polysaccharides staining) (ScyTek Laboratories), and Amyloid Stain Kit (Congo Red) (for amyloid staining) (ScyTek Laboratories) according to the manufacturer's protocol. Images were acquired using a DP72 CCD camera (Olympus, Tokyo, Japan) mounted on an ECLIPSE E800 (Nikon, Tokyo, Japan), BX53 (Olympus), or BZ-X800 microscope (Keyence, Osaka, Japan). Quantification of tissue images was performed using the hybrid cell count algorithm (Keyence).

Immunostaining and TUNEL staining

Fluorescent immunostaining and diaminobenzidine staining were performed using the following protocol with some modifications[18,28]. Anesthetized adult mice were perfused transcardially with saline solution, followed by 4% PFA in 0.1 M PB (pH 7.4). Livers were dissected and postfixed in the same fixative overnight at 4 °C. Fixed tissues were cryoprotect in 30% sucrose in 0.1 M PB (pH 7.4) overnight at 4 °C and embedded in optimal cutting temperature compound (Sakura Finetek, Torrance, CA, USA). Frozen sections (14 μm thick) were collected on MAS-coated glass slides (Matsunami Glass, Bellingham, WA, USA). Sections were blocked for 2 h with 5% normal goat or donkey serum in 0.1% Triton X-100 in PBS (PBST), followed by incubation with primary antibodies in a blocking buffer at 4 °C overnight. After four washes with PBST, sections were incubated for 2 h with Alexa Fluor 488-, Alexa Fluor 555-, or Alexa Fluor 647-conjugated secondary antibodies (Thermo Fisher Scientific). After counterstaining with 0.7 nM Hoechst 33342 (Thermo Fisher Scientific) for the nucleus, 9 μM Bodipy (Thermo Fisher Scientific) for lipid droplets, or 0.1 μM Acti-stain 555 phalloidin (Cytoskeleton Inc, Denver, CO, USA) for cytoplasmic F-actin, sections were mounted and imaged using a confocal microscope (FV3000, Olympus). Acti-stain 555 phalloidin dye was used to delineate the entire cytoplasmic F-actin, excluding vacuolar structures. To immunostain cultured cells, fixed cells were blocked for 1 h with 5% normal goat or donkey serum in PBST, followed by incubation with primary antibodies in a blocking buffer for 1 h. After three washes with PBST, cells were incubated for 1 h with Alexa Fluor 488-, Alexa Fluor 555-, or Alexa Fluor 647-conjugated secondary antibodies. After counterstaining with 0.7 nM Hoechst 33342, the cells were mounted. To detect apoptosis, TUNEL staining was performed using the In Situ Cell Death Detection Kit, TMR-red (Roche Diagnostics, Basel, Switzerland), according to the manufacturer's instructions.

Extraction of hepatic triglyceride and cholesterol

The total lipid was extracted from the male liver at 9–13 months old, following the Folch method with a minor modification[29]. Each liver sample (~100 mg tissue) was mechanically homogenized in 10 volumes of water using a BioMasher homogenizer (Nippi Inc, Tokyo, Japan). A 440 μL aliquot of the homogenate was vigorously mixed with 1100 μL methanol/chloroform solution (1:2) by vortexing for 2 min, followed by centrifugation at 15,000 × *g* for 5 min at 25 °C. After centrifugation, 400 μL of the organic layer was collected and evaporated at 80 °C. The lipid was dispersed in isopropanol and stored at −20 °C until analysis.

Secretion assay of very-low-density lipoprotein (VLDL) from liver

VLDL Secretion assay was performed following the protocol[30]. Triton WR-1339, an inhibitor of lipoprotein lipase, has been used to quantify hepatic VLDL-triglycerides secretion rate. Control and $Nwd1^{-/-}$ mice were fed a normal diet. After fasting for 2 h, male mice aged 6–12 months were injected with the saline containing Triton WR-1339 (500 mg/kg body weight; MedChenExpress, New Jersey, USA) via the tail vein. Blood samples were obtained from the submandibular vein before and 1 and 2 h after Triton WR-1339 administration. The collected blood was centrifuged at 5000 rpm for 15 min to isolate plasma.

Measurement of triglyceride and cholesterol

Triglyceride and total cholesterol levels were enzymatically measured with Labo Assay Triglyceride (FUJIFILM Wako) and LaboAssay Cholesterol kit (FUJIFILM Wako), respectively, according to the manufacturer's instruction. The colorimetric absorbance at 600 nm ± 10 nm was measured using Nivo Multimode Plate Reader (PerkinElmer, Massachusetts, USA). The triglycerides and total cholesterol content were represented as mg/dL or mg/g tissue.

ER fraction and WB

The ER faction was obtained following the protocols with some modifications[31,32]. Dissected fresh livers were homogenized in fraction buffer containing 10 mM HEPES (pH 7.4), 220 mM mannitol, 90 mM sucrose, and protease inhibitor cocktails (Complete mini, Merck Millipore) using Potter–Elvehjem homogenizers and then further homogenized via passage through a 27-gauge needle. The crude postnuclear supernatant was further clarified via centrifugation twice at 7000 × *g* for 10 min each and then at 10,000 × *g* for 10 min at 4 °C. The pellet and supernatant were collected as the mitochondrial and cytoplasmic fractions, respectively. The cytoplasmic fraction was further separated into an ER-enriched pellet and cytosolic supernatant by ultracentrifugation (Optima LE-80K, Beckman Coulter, Brea, CA, USA) at 100,000 × *g* for 1 h at 4 °C. The ER pellet was resuspended in the fraction buffer, and the total protein concentration was measured using the Bradford method (Bio-Rad, Hercules, CA, USA). For WB, the samples were treated with 2× sample buffer (125 mM Tris-HCl, pH 6.8, 4% SDS, 10% sucrose, and 0.01% bromophenol blue) for 1 h at 37 °C, resolved by 8–12% SDS-PAGE, and electroblotted onto an Immobilon-P membrane (Merck Millipore) using a semidry transfer apparatus. After blocking with 1–5% skim milk in TBST (150 mM NaCl, 10 mM Tris-HCl, pH 7.4, 0.1% Tween 20), membranes were incubated with primary antibody for 1 h, followed by incubation with horseradish peroxidase (HRP)-conjugated secondary antibody (Cytiva [Marlborough, MA, USA] or Jackson ImmunoResearch [West Grove, PA, USA]). The signal was detected using Immobilon Western chemiluminescent HRP substrate (Merck Millipore). Blot images were captured using the Fusion Solo S system (Vilber Lourmat, Marne La Vallée, France) and quantified using the Quantification Software Module (Vilber Lourmat).

Proteomic analysis and protein binding assay

HEK293T cells expressing Halo-Nwd1 were washed with ice-cold PBS and lysed in lysis buffer containing 50 mM Tris-HCl (pH 7.4), 150 mM NaCl, 1 mM EDTA, 1% NP-40, and protease inhibitor cocktail for 15 min at 4°C. The lysate was diluted 4-fold with Halo tag protein purification buffer containing 1× PBS, 1 mM DTT, and 0.005% NP-40 (Nacalai Tesque, Kyoto, Japan). The lysate was centrifuged at 15,000 rpm for 10 min at 4 °C, and the supernatant was incubated with HaloLink Resin (Promega) overnight at 4 °C. After brief centrifugation, the pelleted resin was washed four times with Halo tag protein purification buffer. To determine the proteins interacting with Halo-Nwd1, the pelleted resin was treated with 2× sample buffer for 1 h at 37 °C and resolved by SDS-PAGE. The gel was stained using a Silver Stain MS Kit (FUJIFILM Wako Pure Chemical) according to the manufacturer's instructions. Gel slices containing the protein bands were excised for proteomic analysis on a nanoLC-MS/MS system (Japan Proteomics Inc., Tokyo, Japan). Mass data acquisitions and peptide identification were performed using Mascot software. To verify the purification of recombinant halo-Nwd1 protein, the resin crosslinked with Halo-Nwd1 was incubated with HaloTEV protease (Promega) overnight at 4 °C. Eluted Nwd1 protein was resolved by SDS-PAGE, followed by Coomassie brilliant blue (CBB) staining. For the protein binding assay, HEK293T cells expressing Halo-Nwd1 along with Flag-SERCA2, Flag-SERCA2-N, or Flag-SERCA2-C were lysed and purified using HaloLink Resin. Halo-Nwd1-binding proteins were treated with 2× sample buffer for 1 h at 37 °C and resolved by SDS-PAGE, followed by WB using anti-Flag antibody.

Quantitative PCR

Quantitative PCR was performed following the protocol[33]. Total RNA prepared from adult mouse livers was reverse-transcribed using a PrimeScript II first-strand cDNA Synthesis Kit (Takara, Shiga, Japan) with a random hexamer primer. According to the manufacturer's protocol, PCR was performed using TB Green Ex Taq II Mix (Takara) and the Thermal Cycler Dice Real-Time System (Takara). The primer set used for qPCR was as follows: Nwd1; forward primer, 5′-CACCTAGCAAAGAGCT GCTGCG; reverse primer, 5′-GAATTCAGCTAGCACGCCATGCCT C-3′, Perk; forward primer, 5′-CGTGACCCATCTGCACTAAT-3′, reverse primer, 5′-TCCCTAGACCACCTGAAGAA-3′[34], eIF2a; forward primer, 5′-CACCGCTGTTGACAGTCAGAG-3′, reverse primer, 5′-GCAAAC AATGTCCCATCCTTACT-3′[35], Atf4; forward primer, 5′-GCAAGG AGGATGCCTTTTC-3′, reverse primer, 5′-GTTTCCAGGTCATC CATTCG-3′[36], Chop; forward primer, 5′-CACATCCCAAAGCCCTCGC TCTC-3′, reverse primer, 5′-TCATGCTTGGTGCAGGCTGACCAT-3′[36], Gadd34; forward primer, 5′-CTTTTGGCAACCAGAACCG-3′, reverse primer, 5′-CAGAGCCGCAGCTTCTATCT-3′[36], Grp78; forward primer, 5′-TCAGCATCAAGCAAGGATTG-3′, reverse primer, 5′-AAGCCGT GGAGAAGATCTGA-3′[36], Xbp1(total); forward primer, 5′-AAGAAC ACGCTTGGGAATGG-3′, reverse primer, 5′-ACTCCCCTTGGCCTC CAC-3′[36], Xbp1(splicing); forward primer, 5′-GAGTCCGCAGCAGGT G-3′, reverse primer, 5′-GTGTCAGAGTC-CATGGGA-3′[36], Atf6; forward primer, 5′-TAGTTCTCAGTCCCCCCTTT-3′, reverse primer, 5′-CCAT GTTCTGTTTTGTTTCC-3′[37], Edem1; forward primer, 5′-GGGACCAAG AGGAAAAGTTTG-3′, reverse primer, 5′-GAGGTGAGCAGGTCAA ATCAA-3′[36], Grp94; forward primer, 5′-AGTCGGGAAGCAACAGAG AA-3′, reverse primer, 5′-TCTCCATGTTGCCAGACCAT-3′[37], Ire1α; forward primer, 5′-TCACCATTGGAGACAAAGGAGAGTG-3′, reverse primer, 5′-TGGGCAGGTTGTTAGGAAATCTCTC-3′[37], IL6; forward primer, 5′-TGATGCACTTGCAGAAAACA-3′, reverse primer, 5′-AC CAGAGGAAATTTTCAATAGGC-3′[38], IL1β; forward primer, 5′-GGAC CCATATGAGCTGAAAGCT-3′, reverse primer, 5′-TGTCGTTGCTT GGTTCTCCTT-3′[38], Tgfb; forward primer, 5′-TCGAGGGCGAGAG AAGTTTA-3′, reverse primer, 5′-AAAAGAATGTCCCGGCTCTC-3′[38], Tnfa; forward primer, 5′-AGGGTCTGGGCCATAGAACT-3′, reverse primer, 5′-CCACCACGCTCTTCTGTCTAC-3′[38], β-actin; forward primer, 5′-GGCTGTATTCCCCTCCATCG-3′, reverse primer, 5′-CCAGTTGGT AACAATGCCATGT-3′[33].

ATPase activity measurement

The ATPase activity of SERCA2 was measured using the following protocol with some modifications[16]. The ATPase activity of the ER fraction was measured using a QuantiChrom ATPase/GTPase assay kit (BioAssay Systems, Hayward, CA, USA) following the manufacturer's instructions and quantified as colorimetric absorbance using a Nivo S luminometer (PerkinElmer, Shelton, MA, USA). The SERCA2 protein content in the ER fraction was determined by WB, and ATPase activity was normalized to that of total SERCA2 protein.

Ca^{2+} measurement

The Ca^{2+} concentrations in ER and mitochondrial fractions were measured using the fluorescent indicator Fluo3. Each fraction was treated in buffer containing 100 mM KCl, 10 mM MOPS (pH 7.2), 0.01% Pluronic F-127, 2.6 μM Fluo3 (Dojindo, Kumamoto, Japan) in OptiPlate-96 Black plates (PerkinElmer). The fluorescent intensity (excitation: 495 nm, emission: 530 nm) was measured using a Nivo S luminometer. The total protein content of each fraction was determined using the Bradford method.

Gene Ontology (GO) and Kyoto Encyclopedia of Genes and Genomes (KEGG) analysis

We used "DAVID Bioinformatics Resources"[39,40] to perform Gene Ontology (GO) enrichment analysis (including biological process, cellular component, and molecular function) and Kyoto Encyclopedia of Genes and Genomes (KEGG) pathway enrichment analysis[41].

Statistics and reproducibility

Statistical analyses were performed using Microsoft Excel version 16.77.1 (Microsoft, Redmond, WA, USA) and Prism version 9.5.0 (GraphPad, La Jolla, CA, USA). For each statistical analysis, numerical data from at least three biological replicates ($n = 3$) were used, and all graphs show the mean ± SD. One-way analysis of variance (ANOVA) followed by Welch's *t*-test with Holm–Bonferroni correction was used in multiple-group comparisons. Welch's *t*-test was used to analyze between-group differences for the following variables: Hematoxylin and eosin (H&E)$^+$ normal hepatocytes, oil red O$^+$ area, Sirius red$^+$ fibrotic area, PAS$^+$ area, the number of dead cells in the liver, the result of blood tests, the number of F4/80$^+$ cells, F4/80$^+$ areas, the expression of ER stress-related proteins after tunicamycin (TM) treatment as determined by WB, relative ATPase activity, and relative Ca^{2+} concentrations. The paired *t*-test was used to compare liver and body weights and protein expression between littermates. The chi-squared test was used to compare the number of genotypes in the offspring of *Nwd1*$^{+/-}$ mating pairs. Significance was indicated by $P < 0.05$. We calculated the area of swollen hepatocytes, Oil red O$^+$ area, Sirius red$^+$ fibrotic area, and PAS$^+$ area using hybrid cell count software (Keyence). The number of F4/80-positive cells and the total area occupied by F4/80-positive cells within a 1 mm^2 unit area, excluding non-cellular regions, were quantified using ImageJ. The numbers of lipid droplets and vacuolar structures in the liver were manually measured by polygon selection using cellSens imaging software (Olympus). Lipid droplets that partially filled the vacuole and detached from the vacuolar membrane were classified as type C vacuoles. The area of the vacuoles was measured as the area of the vacuolar structures minus that occupied by the lipid droplets.

Reporting summary

Further information on research design is available in the Nature Portfolio Reporting Summary linked to this article.

Results

Generation of *Nwd1*$^{-/-}$ mice

The mouse Nwd1 gene was mapped to chromosome 8, and it consisted of 19 exons (Fig. 1A). To reveal the in vivo function of *Nwd1*, we generated *Nwd1*$^{-/-}$ mice. *Nwd1*^{flox} mice were generated by CRISPR-Cas9 genome editing using electroporation in zygotes. In total, 320 embryos were transferred to the recipient uteri. Of the 71 offspring born, five floxed mice were obtained. Conditional knockout of the *Nwd1*^{flox} allele generated by genome editing was confirmed by PCR using genomic DNA (Fig. 1A, B). To obtain the mice harboring the *Nwd1*$^{-}$ null allele, heterozygous *Nwd1*$^{flox/+}$ mice were crossed with the CAG-Cre deleter mouse line, which ubiquitously expresses Cre recombinase, thereby allowing deletion of the loxP-flanked genomic region (Fig. 1A). The *Nwd1*$^{-}$ allele lacked the genomic region encompassing exon 5, a pivotal exon encoding the NACHT domain (Fig. 1A). Subsequent interbreeding of the heterozygous mutant mice yielded homozygous mutant (*Nwd1*$^{-/-}$) pups. The accuracy of targeted disruption of *Nwd1* was confirmed through genomic sequencing and PCR (Fig. 1C). Genotyping of 211 adult offspring produced by breeding heterozygous *Nwd1*$^{+/-}$ mice revealed that the number of *Nwd1*$^{-/-}$ mice was 7% lower than expected from the Mendelian ratio (Fig. 1D). A quantitative reverse transcription PCR (qRT-PCR) analysis targeting exon 5 of *Nwd1* mRNA confirmed the absence of *Nwd1* mRNA expression in *Nwd1*$^{-/-}$ liver (Fig. 1E). RT-PCR analysis of *Nwd1*$^{-/-}$ mice further demonstrated the lack of mRNA expression in the region spanning exon 6 to exon 7 (Supplementary Fig. 1A). Immunostaining with Nwd1 antibody also demonstrated that Nwd1 expression was absent in the liver tissue of *Nwd1*$^{-/-}$ mice (Fig. 1F). Notably, the expression pattern of Nwd1 was not homogeneous in wild-type mouse liver. The distribution of Nwd1 expression in hepatic lobes exhibited a patchy pattern, with regions displaying high levels of expression interspersed with regions exhibiting low levels (Fig. 1F). This observation indicates that Nwd1 expression may fluctuate in response to the status of hepatocytes under normal physiological conditions. Histological examination demonstrated that most *Nwd1*$^{-/-}$ adult mice exhibited normal development and no evident abnormalities in any organs, excluding the liver and lungs. The livers of *Nwd1*$^{-/-}$ mice showed an ~1.4-fold increase in liver size versus that in wild-type mice (wild-type, 1.5 ± 0.4; *Nwd1*$^{-/-}$, 2.1 ± 0.4) despite no significant differences in body weight (wild-type, 29.0 ± 5.9; *Nwd1*$^{-/-}$, 30.2 ± 5.2; Fig. 1G–I, Supplementary Fig. 1B). Gross observation revealed abnormal speckled fatty-like patterns (Fig. 1G, arrowheads) and white fibrotic-like structures (Fig. 1G, arrows) on the surface of *Nwd1*$^{-/-}$ hepatic lobes.

The *Nwd1*$^{-/-}$ liver exhibits MASH-like pathology

H&E staining of *Nwd1*$^{-/-}$ livers revealed a striking increase in the number of enlarged and lucent hepatocytes with a lack of eosin staining compared to the findings in wild-type littermates (wild-type, 12.0% ± 9.3%; *Nwd1*$^{-/-}$, 30.6% ± 10.6%; Fig. 2A, B). These swollen hepatocytes did not appear to have undergone programed cell death because their nuclei were not contracted or fragmented (Fig. 2A). We next performed oil red O staining on the liver tissues to detect the neutral lipid content in hepatocytes, finding that the size of the positively stained area was substantially increased in *Nwd1*$^{-/-}$ livers (wild-type, 0.5% ± 0.4%; *Nwd1*$^{-/-}$, 13.0% ± 2.6%). Many lipid droplets, storage organelles for neutral lipids, accumulated in a zonate pattern around the central vein in the *Nwd1*$^{-/-}$ hepatic lobule (Fig. 2C, D). We further assessed the organization of collagen fibers in tissues using Sirius red staining. As presented in Fig. 2E, F, *Nwd1*$^{-/-}$ mice exhibited severe collagen fiber deposition in their livers (wild-type, 2.0% ± 1.1%; *Nwd1*$^{-/-}$, 9.2% ± 6.5%), indicating that the loss of *Nwd1* resulted in abnormal fibrosis that resembled MASH. Congo red staining (Supplementary Fig. 2A) illustrated that *Nwd1*$^{-/-}$ mouse livers did not accumulate amyloid fibrils, an extracellular deposition of amyloid proteins frequently observed in hepatic amyloidosis. PAS staining, which detects polysaccharides such as glycogen and mucosubstances such as glycoproteins and mucins, was significantly reduced in swollen *Nwd1*$^{-/-}$ hepatocytes (wild-type, 98.2% ± 0.15%; *Nwd1*$^{-/-}$, 61.5% ± 18.6%; Fig. 2A and Supplementary Fig. 2B, C). Because pretreatment with α-amylase abolished PAS staining in liver sections, insoluble glycogen was not accumulated in the *Nwd1*$^{-/-}$ mouse liver (Supplementary Fig. 2B).

Based on the swelling of hepatocytes and detection of fibrosis, we explored the possibility of accelerated apoptosis in the *Nwd1*$^{-/-}$ liver using double staining with anti-cleaved caspase-3 antibody and TUNEL staining. As presented in Fig. 2G, although many TUNEL$^+$ cells were observed in *Nwd1*$^{-/-}$ livers (wild-type, 8.7% ± 8.6%; *Nwd1*$^{-/-}$, 49.2% ± 19.2%), few caspase-3$^+$ apoptotic cells were found in these livers (wild-type, 0.1% ± 0.2%; *Nwd1*$^{-/-}$, 0.5% ± 0.5%). TUNEL staining is known to detect different types of cell death[42], including pyroptosis, a form of programed necrotic cell death activated upon inflammation[43,44]. A much larger percentage of cells was positive for cleaved caspase-1, a pyroptosis marker, in *Nwd1*$^{-/-}$ mouse livers (wild-type, 11.7% ± 9.6%; *Nwd1*$^{-/-}$, 41.7% ± 12.3%; Fig. 2H, I), indicating accelerated pyroptosis. The observation that *Nwd1*$^{-/-}$ hepatocytes lacked nuclear fragmentation, a morphological sign of apoptosis, was also consistent with the observation of inflammatory pyroptosis in *Nwd1*$^{-/-}$ livers. To evaluate the inflammatory response and lipid metabolism, hematological and biochemical analyses were performed using serum and peripheral whole blood. The total number of leukocytes was ~3-fold higher in *Nwd1*$^{-/-}$ mice than in wild-type mice (relative ratio = 2.9 ± 1.0; Fig. 2J). Although *Nwd1*$^{-/-}$ mice had increased counts of each type of leukocytes, including monocytes (relative ratio = 3.7 ± 2.3; Fig. 2J), lymphocytes, neutrophils, eosinophils, and basophils, the proportion of each cell type was unchanged (Supplementary Fig. 2D, E). The pathological phenotype of *Nwd1*$^{-/-}$ mice, including hepatomegaly, excessive lipid accumulation in hepatocytes, fibrosis, and inflammatory pyroptosis, closely resembled that of MASH. In general, liver inflammation is often involved in the pathogenesis of MASH. Activation of Kupffer cells, resident macrophages of the liver, is associated with hepatic inflammation through the release of an array of inflammatory mediators and reactive oxygen species. We examined whether *Nwd1*$^{-/-}$ liver develops the inflammation using an antibody to F4/80, a marker for Kupffer cells. No significant difference was observed in the mean number of F4/80-positive cells per unit area, GOT,

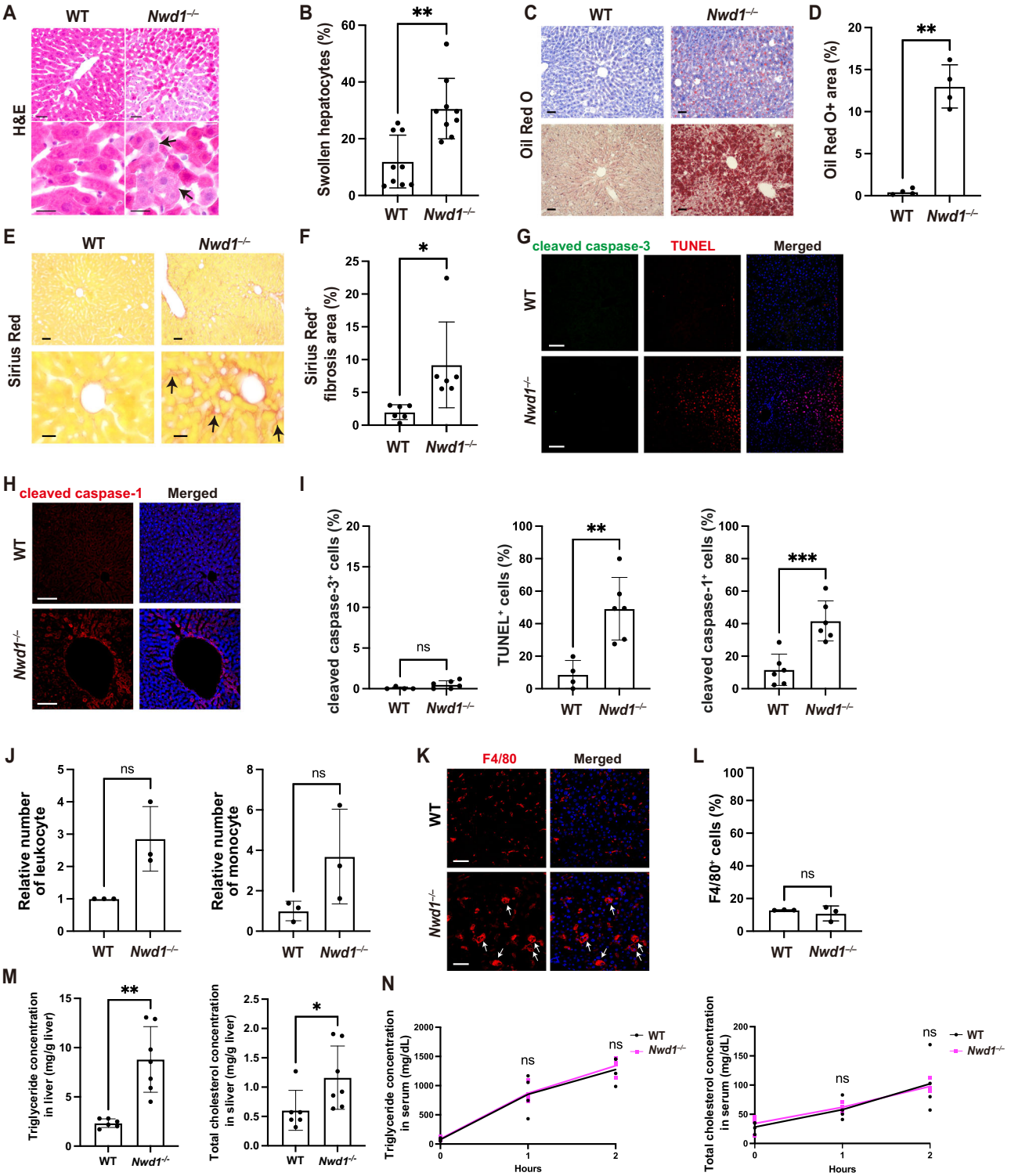

Fig. 2 | MASH-like phenotype in the adult *Nwd1*$^{-/-}$ mouse liver. **A**–**I** Histological analyses of the 2–7-month-old male and female mouse liver. H& E (**A**, **B**), oil red O (**C**, **D**), and Sirius red (**E**, **F**) staining of *Nwd1*$^{-/-}$ or wild-type livers. Nuclei were counterstained with hematoxylin (**C**, upper). Welch's *t*-test was used to compare the number of swollen hepatocytes (%) ($n = 9$) (**B**), oil red O^{+} area (%) ($n = 4$) (**D**), and Sirius red^{+} fibrotic area (%) ($n = 6$) (**F**). Arrows denote swollen hepatocytes in (**A**) and Sirius red^{+} fibrotic pathology in (**E**). **G** Double staining with anti-cleaved caspase-3 antibody (*green*) and TUNEL (*red*). **H** Immunostaining using anti-cleaved caspase-1 (*red*) antibody. Nuclei were stained with Hoechst dye (*blue*). **I** Comparison of the number of cleaved caspase-3^{+} cells (%), TUNEL^{+} cells (%), and cleaved caspase-1^{+} cells (%). Welch's *t*-test, WT: $n = 4$, *Nwd1*$^{-/-}$: $n = 6$. **J** Analysis of leukocyte and monocyte counts in peripheral blood (relative number) of 5–9 month-old male and female mice. Welch's *t*-test, $n = 3$. **K** Liver tissues of 12-month-old male mice immunostained with anti-F4/80 (*red*). Nuclei were stained with Hoechst dye (*blue*). **L** Mean number of F4/80^{+} cells of total hepatocytes in 10–12-month-old male livers (%) (Welch's *t*-test, $n = 3$). **M** Triglycerides and total cholesterol content in 9–13 month-old male *Nwd1*$^{-/-}$ or wild-type livers. Welch's *t*-test, WT: $n = 6$, *Nwd1*$^{-/-}$: $n = 7$. **N** Triglycerides secretion into the peripheral blood after the Triton WR-1339 administration. Triglycerides and total cholesterol levels in the plasma of 7–11-month-old male and female mice were measured before (0) and 1 and 2 h after the Triton WR-1339 injection. Welch's *t*-test, $n = 4$. ns, not significant; *, $P < 0.05$; **, $P < 0.01$; ***, $P < 0.001$. Black and magenta dots represent each independent biological replicate, and all graphs show the mean ± SD. Scale bars, 40 (**A** [upper]), 20 (**A** [lower]) and (**E** [lower]), 50 (**C**, **E** [upper] and **K**), or 100 μm (**G**, **H**).

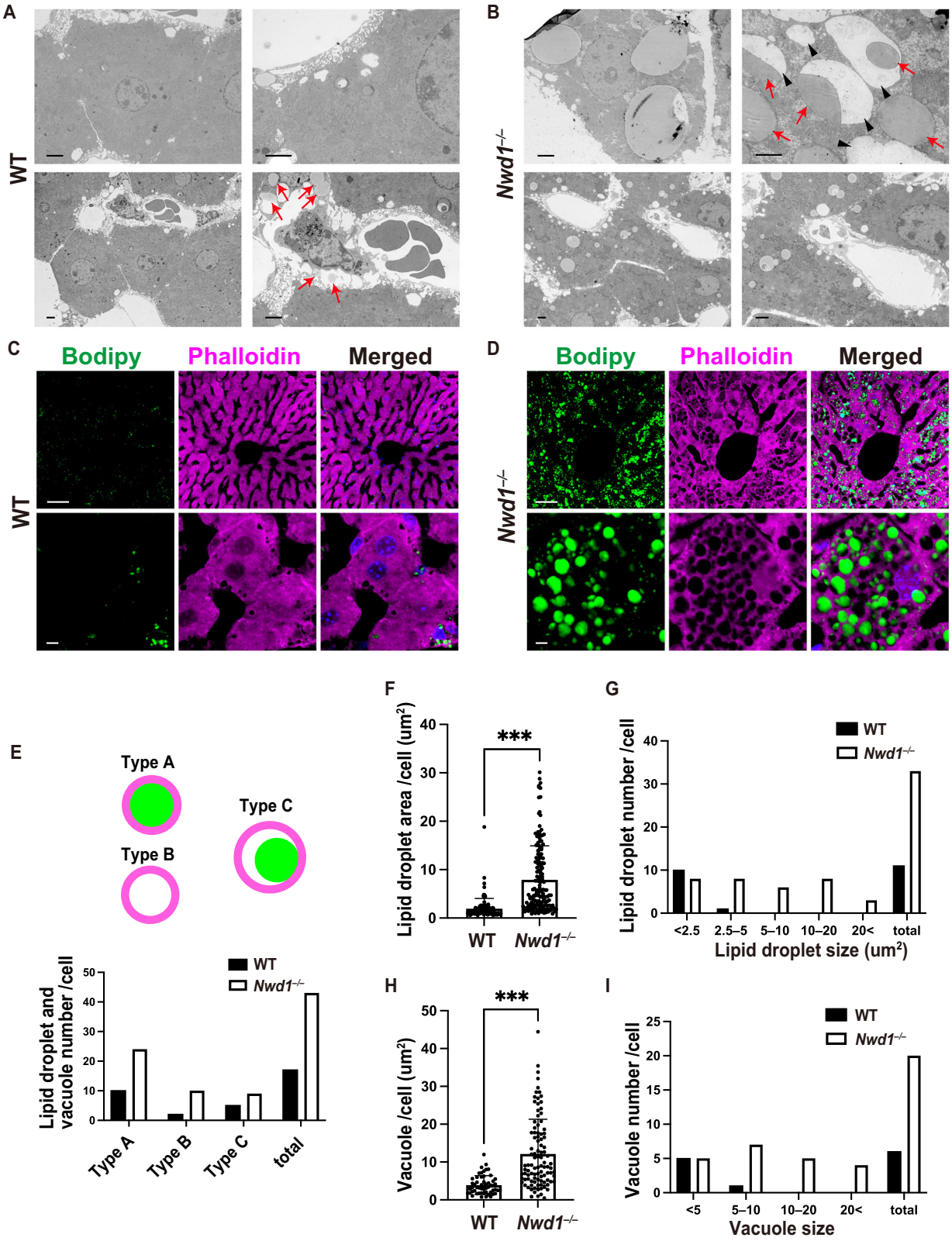

and GPT levels (Fig. 2L, Supplementary Fig. 2I). However, detailed microscopic analysis revealed that individual macrophages in *Nwd1*$^{-/-}$ liver were hypertrophied, characterized by a swollen cytoplasm and irregular ameboid morphology, compared to those in wild-type liver (relative ratio = 2.3 ± 0.1) (Fig. 2K, Supplementary Fig. 2F, G), suggesting the activation of resident Kupffer cells in *Nwd1*$^{-/-}$ liver.

To explore the mechanism of lipid accumulation in *Nwd1*$^{-/-}$ liver, we first measured triglycerides and cholesterol levels in the liver. As shown in Fig. 2M, *Nwd1*$^{-/-}$ liver had a significantly higher accumulation of both triglycerides and total cholesterol [triglycerides (mg/g of tissue); wild-type, 2.3 ± 0.4; *Nwd1*$^{-/-}$, 8.8 ± 3.3, total cholesterol (mg/g of tissue); wild-type, 0.6 ± 0.3; *Nwd1*$^{-/-}$, 1.2 ± 0.5]. Lipid analysis revealed that the total content

Fig. 3 | Accumulation of lipid droplets and vacuolar structures in *Nwd1*$^{-/-}$ hepatocytes. Electron microscopy of 2–7-month-old male wild-type (**A**) and *Nwd1*$^{-/-}$ (**B**) mouse liver. Arrows in (**A**) indicate the secretion of lipid droplets from hepatocytes into the wild-type liver sinusoid. **B** *Nwd1*$^{-/-}$ hepatocytes contained numerous large vacuolar structures (black arrowheads) partially or entirely filled with electron-dense lipid droplets (red arrows). Lipid droplet staining with Bodipy dye (*green*) in 2–7-month-old male wild-type (**C**) and *Nwd1*$^{-/-}$ livers (**D**). Cytoplasmic F-actin was stained with phalloidin (*magenta*), and nuclei were counterstained with Hoechst dye (*blue*). **E** Vesicular structures observed in *Nwd1*$^{-/-}$ hepatocytes were classified into three types: type A, a typical lipid droplet surrounded by a membrane; type B, a vacant vacuole lacking Bodipy^{+} lipids; and type C, a lipid droplet partially or fully detached from the surrounding vacuolar membrane. The bars denote the distributions of types A, B, and C vesicles in wild-type and *Nwd1*$^{-/-}$ hepatocytes. **E–I** Quantification of the area occupied by lipid droplets (WT: $n = 112$, *Nwd1*$^{-/-}$: $n = 163$) (**F**), the number and size of lipid droplets (**G**), the area occupied by vacuolar space (WT: $n = 54$, *Nwd1*$^{-/-}$: $n = 100$) (**H**), and the number of vacuoles (**I**) in 2–7-month-old male wild-type and *Nwd1*$^{-/-}$ hepatocytes. Welch's *t*-test, ***, $P < 0.001$. Black dots represent individual value, and all graphs show the mean ± SD. Scale bars, 2 (**A**, **B**), 50 (**C** [upper] and **D** [upper]), or 5 μm (**C** [lower] and **D** [lower]).

of triglycerides (relative ratio = 1.0 ± 0.3) and cholesterol (relative ratio = 0.9 ± 0.2) in the peripheral serum remained unchanged (Supplementary Fig. 2H) despite the lipid accumulation in *Nwd1*$^{-/-}$ livers, suggesting impairment of the lipid droplet efflux in *Nwd1*$^{-/-}$ mice. To assess whether *Nwd1*$^{-/-}$ mice exhibit a deficiency in the fat excretion from the liver into the peripheral blood, the hepatic VLDL-triglycerides secretion rate was determined after administering Triton WR-1339 via the tail vein. *Nwd1*$^{-/-}$ mice and wild-type mice exhibited nearly identical rates of increase in peripheral blood triglycerides and total cholesterol following Triton WR-1339 administration (Fig. 2N), indicating that the excretion of fat stored in hepatocytes is not stimulated. Given the unchanged fat levels in the peripheral blood, it is highly likely that the clearance of accumulated lipid droplets is suppressed in the livers of *Nwd1*$^{-/-}$ mice. Consistently, lipid droplets in the *Nwd1*$^{-/-}$ liver were rarely observed in the sinusoids, the pathway for their egress from hepatocytes as described below.

In addition to the liver, we performed histological analysis of various organs. *Nwd1*$^{-/-}$ mouse lungs featured flattened alveoli (Supplementary Fig. 3). We observed no abnormalities in the structure or tissue architecture of the heart, intestine, kidneys, skeletal muscle, spleen, testes, and white adipose tissue (Supplementary Fig. 3).

Accumulation of lipid droplets and ER-derived vacuoles in *Nwd1*$^{-/-}$ hepatocytes

Ultrastructure analysis using electron microscopy revealed that *Nwd1*$^{-/-}$ hepatocytes were occupied by numerous vesicular structures. These cytoplasmic vesicles varied in size and were divided into two types based on the inner structure: gray vesicles filled with electron-dense material and vacuoles that appeared vacant or contained small amounts of lipid (Fig. 3A, B). Ultrastructurally, both types of vesicles were surrounded by a single membrane (Fig. 3B). Based on these morphological characteristics, we concluded that the gray vesicles filled with electron-dense materials corresponded to the lipid droplets stained with oil red O. Notably, many tiny lipid droplets were evident in the wild-type liver sinusoid (Fig. 3A, arrows). However, we rarely observed lipid droplets in the *Nwd1*$^{-/-}$ sinusoid (Fig. 3B). To distinguish the vesicles, Bodipy staining of lipid droplets was performed in conjunction with phalloidin staining. Consistent with the result of electron microscopy, *Nwd1*$^{-/-}$ hepatocytes contained many vacant vacuoles in addition to lipid droplets filled with Bodipy^{+} triglycerides (Fig. 3C, D). We classified the vesicular structures based on Bodipy staining into three types (Fig. 3E): type A, a typical lipid droplet surrounded by a membrane; type B, a vacant vacuole lacking Bodipy^{+} lipids; and type C, a vacuole containing a small amount of Bodipy^{+} lipids, representing a transitional morphology between types A and B. The *Nwd1*$^{-/-}$ liver exhibited increases levels of all subtypes (Fig. 3E). Quantification of the areas occupied by lipid droplets and vacuoles in a single hepatocyte revealed a significant increase in both lipid droplets (wild-type, 2.0 ± 2.1 μm^2; *Nwd1*$^{-/-}$, 8.0 ± 7.0 μm^2) and vacuolar structures (wild-type, 4.0 ± 2.5 μm^2; *Nwd1*$^{-/-}$, 12.2 ± 9.1 μm^2) in *Nwd1*$^{-/-}$ mice (Fig. 3F, H). The numbers of giant lipid droplets larger than 2.5 μm^2 (Fig. 3G) and vacuoles larger than 5 μm^2 (Fig. 3I) were significantly increased in *Nwd1*$^{-/-}$ mice. Based on the increased size and number of lipid droplets, the absence of lipid droplets in the sinusoids (Fig. 3B), and the unchanged levels of total triglycerides and cholesterols in peripheral blood (Supplementary Fig. 2H), we assumed that *Nwd1*$^{-/-}$ mice have defective lipid droplet efflux from the sinusoids, in addition to increased lipid synthesis in hepatocytes.

From where do these empty vacuoles originate? Previous studies revealed that lipid droplet biogenesis is initiated at the ER, and ER-derived membrane structures enclose the lipid during the maturation of lipid droplets[12,16,45–47]. Cells lacking SEIPIN/BSCL2, a protein localized to ER–lipid droplet contact sites, had fewer ER–lipid droplet contact sites, and the transport of lipid droplets occurred independently of the ER[12]. Immunostaining for SEIPIN demonstrated that the *Nwd1*$^{-/-}$ liver exhibited normal SEIPIN^{+} zonation surrounding the central vein, and the area of SEIPIN^{+} zonation remained unchanged (Supplementary Fig. 4A). Hepatocytes play distinct metabolic roles depending on their specific location along the lobular postcentral axis. This regional segregation of hepatocytes is called zonation. Consistently, the accumulation pattern of Bodipy^{+} lipid droplets within *Nwd1*$^{-/-}$ hepatic lobules appeared to be distributed as hepatic zonation surrounding a central vein (Supplementary Fig. 4A). Immunostaining for the ER marker KDEL illustrated that many vacuoles in *Nwd1*$^{-/-}$ hepatocytes were surrounded by KDEL^{+} membranes, supporting that they were derived from the ER (Fig. 4I). The vacuolar structures did not express LC3A/B, indicating that they are unrelated to the autophagy (Supplementary Fig. 4B).

Elevated ER stress in the *Nwd1*$^{-/-}$ liver

We examined the expression of proteins associated with ER and other intracellular organelles, including mitochondria, endosomes, and lysosomes. Notably, the ER membrane proteins SERCA2 and SEIPIN were upregulated in the *Nwd1*$^{-/-}$ liver compared to their wild-type expression (Fig. 4A, B). We confirmed that the *Nwd1*$^{-/-}$ liver exhibited elevated expression of a 100-kDa KDEL protein (Fig. 4A, B). The comparable upregulation was obtained in ER fraction prepared from wild-type and *Nwd1*$^{-/-}$ livers (Supplementary Fig. 5A). Conversely, the expression of ADP/ATP translocase 2 (ANT2) and VDAC, which are proteins of the inner and outer mitochondrial membranes, respectively, remained unchanged in the *Nwd1*$^{-/-}$ liver (Fig. 4A, B). RAB5 and LAMP1 expression was slightly increased in the *Nwd1*$^{-/-}$ liver, whereas RAB7 and LC3A/B expression remained unchanged (Fig. 4A, B). These results suggested that at least two ER-related proteins were upregulated in the *Nwd1*$^{-/-}$ mouse liver.

Because the induction of ER stress is known to be accompanied by increased expression of ER-localized proteins such as KDEL proteins, it was speculated that ER stress was enhanced in the livers of *Nwd1*$^{-/-}$ mice. A previous study illustrated that tunicamycin (TM) treatment induced ER stress in vivo and the development of vacuolar structures in the mouse liver[48]. To assess the susceptibility of *Nwd1*$^{-/-}$ mice to ER stress, we intraperitoneally administered TM into wild-type and *Nwd1*$^{-/-}$ adult mice. Although wild-type mice survived up to 48 h after TM injection, 40% of *Nwd1*$^{-/-}$ mice died within 48 h (Fig. 4C), postulating that *Nwd1*$^{-/-}$ mice were more vulnerable to ER stress or that the basal level of ER stress was already elevated in these mice. To directly evaluate whether ER stress is elevated in the livers of *Nwd1*$^{-/-}$ mice, the ER fraction was isolated from wild-type and *Nwd1*$^{-/-}$ livers following treatment treated with or without TM, and the expression of ER stress-related proteins was quantified by Western blotting. KDEL proteins harboring ER localization signal sequences are known to be upregulated upon the induction of ER stress, and

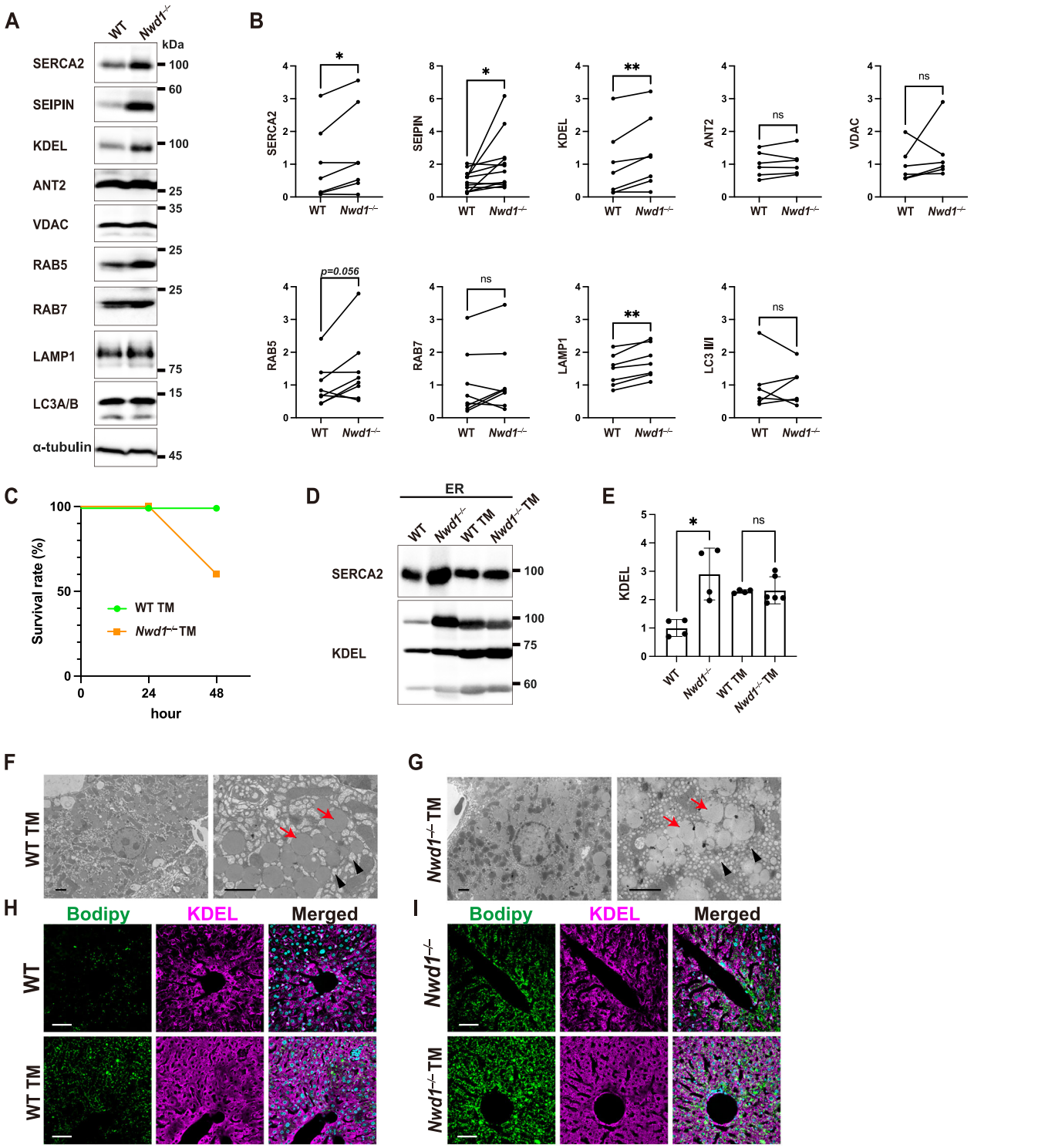

Fig. 4 | Increased ER stress in *Nwd1*$^{-/-}$ livers. A WB of wild-type and *Nwd1*$^{-/-}$ livers from 3–9 month-old males and females using the indicated antibodies. The blot was probed with anti-α-tubulin antibody to confirm equal loading. **B** Quantitative comparison of protein expression between an *Nwd1*$^{-/-}$ mouse and its wild-type littermate (paired *t*-test, $n = 6$–12). **C** Survival curves of 3-month-old *Nwd1*$^{-/-}$ ($n = 10$) and wild-type ($n = 6$) mice after TM treatment. **D** WB of SERCA2 and KDEL proteins in ER fractions prepared from livers with or without TM treatment. **E** Quantitative comparison of the expression of KDEL protein in **D**. One-way ANOVA followed by Welch's *t*-test with Holm–Bonferroni correction (WT: $n = 4$, *Nwd1*$^{-/-}$: $n = 4$, WT TM: $n = 4$, *Nwd1*$^{-/-}$ TM: $n = 6$). ns, not significant; *, $P < 0.05$; **, $P < 0.01$. Black dots represent each independent biological replicate, and the graph shows the mean ± SD. **F**, **G** Electron microscopy of 3-month-old *Nwd1*$^{-/-}$ and wild-type hepatocytes treated with TM. After TM treatment, a significantly increased number of small vacuoles (black arrowheads) and large lipid droplets (red arrows) were observed in both wild-type and *Nwd1*$^{-/-}$ livers. **H**, **I** Lipid (Bodipy, *green*) and ER (anti-KDEL, *magenta*) staining of wild-type and *Nwd1*$^{-/-}$ livers with or without TM treatment. Nuclei were counterstained with Hoechst dye (*cyan*). Scale bars, 2 μm (**F**, **G**), 50 μm (**H**, **I**).

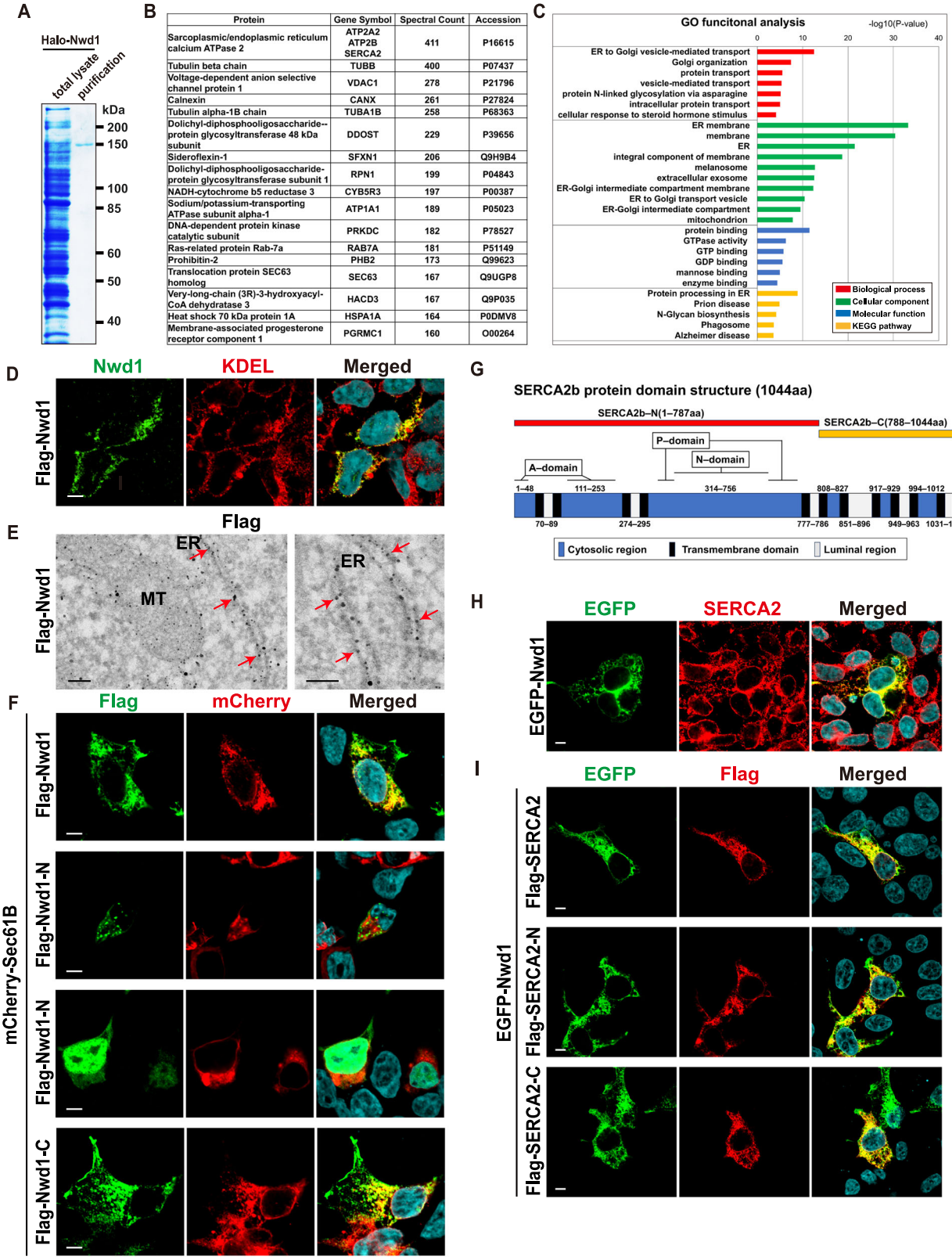

Protein	Gene Symbol	Spectral Count	Accession
Sarcoplasmic/endoplasmic reticulum calcium ATPase 2	ATP2A2 ATP2B SERCA2	411	P16615
Tubulin beta chain	TUBB	400	P07437
Voltage-dependent anion selective channel protein 1	VDAC1	278	P21796
Calnexin	CANX	261	P27824
Tubulin alpha-1B chain	TUBA1B	258	P68363
Dolichyl-diphosphooligosaccharide--protein glycosyltransferase 48 kDa subunit	DDOST	229	P39656
Sideroflexin-1	SFXN1	206	Q9H9B4
Dolichyl-diphosphooligosaccharide-protein glycosyltransferase subunit 1	RPN1	199	P04843
NADH-cytochrome b5 reductase 3	CYB5R3	197	P00387
Sodium/potassium-transporting ATPase subunit alpha-1	ATP1A1	189	P05023
DNA-dependent protein kinase catalytic subunit	PRKDC	182	P78527
Ras-related protein Rab-7a	RAB7A	181	P51149
Prohibitin-2	PHB2	173	Q99623
Translocation protein SEC63 homolog	SEC63	167	Q9UGP8
Very-long-chain (3R)-3-hydroxyacyl-CoA dehydratase 3	HACD3	167	Q9P035
Heat shock 70 kDa protein 1A	HSPA1A	164	P0DMV8
Membrane-associated progesterone receptor component 1	PGRMC1	160	O00264

they have been used as markers of ER stress[49,50]. As presented in Fig. 4D, E, TM administration to wild-type mice increased the expression of KDEL proteins, confirming that TM treatment induces ER stress in hepatocytes. At this time, the levels of these proteins were elevated in the ER fraction of *Nwd1*$^{-/-}$ livers regardless of TM treatment (wild-type, 1.0 ± 0.3; *Nwd1*$^{-/-}$, 2.9 ± 0.9; wild-type with TM treatment, 2.3 ± 0.1; *Nwd1*$^{-/-}$ with TM treatment, 2.3 ± 0.5). Electron microscopy revealed that TM-mediated ER stress drove the accumulation of large lipid droplets and vacuoles in the wild-type liver (Fig. 4F). This hepatic pathology closely resembled that in the *Nwd1*$^{-/-}$ liver without TM administration (Figs. 3B and 4G). Bodipy staining confirmed that TM-mediated ER stress accelerated the accumulation of lipid droplets in wild-type and *Nwd1*$^{-/-}$ livers (Fig. 4H, I). ER stress

Fig. 5 | Nwd1 binds to SERCA2. A Purification of Halo-Nwd1 recombinant protein expressed in HEK293T cells. CBB staining of the SDS-PAGE gel of the cell lysate and purified protein. **B** Identification of Halo-Nwd1-binding proteins by nanoLC-MS/MS. The list of representative Nwd1-binding proteins presents the gene symbols, spectral counts in proteomic analysis, and UniProt database entry numbers. **C** GO enrichment and KEGG pathway analyses of Nwd1-binding proteins. **D** HEK293T cells expressing Flag-Nwd1. ICC with anti-Nwd1 (*green*) and anti-KDEL (*red*) antibodies, revealing the colocalization of Nwd1 with the ER. **E** Immunoelectron microscopy showing the localization of Flag-Nwd1 in the vicinity of the ER. HeLa cells were transfected with Flag-Nwd1 and immunostained with anti-Flag antibody (gold particle). Arrows indicate the Nwd1 signals on or near the ER membranes. MT, mitochondria. **F** Analysis of the Nwd1 region required for localization to the ER. HEK293T cells were transfected with mCherry-Sec61B and Flag-Nwd1, Flag-Nwd1-N, or Flag-Nwd1-C. Cells were stained with anti-Flag (*green*) antibody. **G** Structure and topology of mouse SERCA2b protein (1044 amino acids, accession number NP_733765.1). Blue boxes denote the cytosolic regions comprising the A (amino acids 1–43 and 124–235), N (amino acids 360–600), and P domains (amino acids 330–359 and 601–739), which are involved in ATPase activity. Black boxes denote 11 transmembrane domains, and white boxes denote the ER luminal regions. The red and yellow lines represent SERCA2b–N (amino acids 1–787) and SERCA2b–C (amino acids 788–1044), the deletion mutants of SERCA2b produced in this study. **H** Colocalization of Nwd1 and SERCA2 at the ER. HEK293T cells were transfected with EGFP-Nwd1 and stained with anti-SERCA2 (*red*) antibody. **I** HEK293T transfected with EGFP-Nwd1 and Flag-SERCA2, Flag-SERCA2-N, or Flag-SERCA2-C were stained with anti-Flag (*green*) antibody. Scale bars, 5 μm (**D**, **F**, **H**, **I**) or 100 nm (**E**).

is regulated by several ER transmembrane sensor proteins, including the activating transcription factor 6 (ATF6), inositol-requiring enzyme 1 alpha (IRE1α), and protein kinase R-like endoplasmic reticulum kinase (PERK)[51]. However, qPCR analysis revealed no significant upregulation of mRNAs associated with ATF6, PERK (Perk, eIF2a, Atf4), or IRE1 signaling (Ire1a, spliced Xbp1) in *Nwd1*$^{-/-}$ livers (Supplementary Fig. 5B).

Nwd1 interacts with ER-associated proteins, including SERCA2

To understand the molecular mechanism underlying ER stress induced by Nwd1 depletion, Nwd1-binding proteins were screened using the pulldown assay and proteomic analysis. Nwd1-interacting proteins were copurified with halo-tagged Nwd1 protein from HEK293T cell lysate (Fig. 5A). Proteomic analysis using nanoLC-MS/MS identified 107 proteins as candidate Nwd1-binding proteins, including SERCA2, the mitochondrial outer membrane proteins VDAC1 and sideroflexin-1, the endosome membrane protein RAB7A, and chaperone proteins including calnexin and heat shock 70 kDa protein 1A (Fig. 5B and Supplementary Table 1). GO analysis for biological processes suggested a predominant role of Nwd1 in protein transport (Fig. 5C). According to the predicted distribution of the cellular components and the prediction of molecular function, many Nwd1-binding proteins were expected to localize to the ER membrane and various organelle membranes and function in protein binding (Fig. 5C). In silico pathway analysis using the KEGG database predicted that many Nwd1-binding proteins were involved in protein processing at the ER (Fig. 5C). Collectively, these analyses strongly predicted the involvement of Nwd1 in the membrane transport or processing of ER proteins.

We examined whether Nwd1 is distributed at the ER. Double immunostaining demonstrated the colocalization of Nwd1 and KDEL in cultured HEK293T cells (Fig. 5D). To analyze the association between Nwd1 and ER at higher resolution, immunoelectron microscopy was performed using HeLa cells expressing Flag-Nwd1. As presented in Fig. 5E, many Flag-Nwd1 signals were detected on and near the surface of the ER membrane but rarely in the lumen of the ER, confirming the close association of Nwd1 with the ER membrane. To identify the protein region responsible for ER localization, deletion mutants of Nwd1 were introduced into cultured cells together with mCherry-Sec61B to visualize the ER architecture[27,33]. The overlapping distribution of Flag-tagged full-length Nwd1 and mCherry-Sec61B verified the predominant localization of Nwd1 to the ER. Flag-Nwd1-N, which lacks the central NACHT domain and C-terminal WD40 repeat domain, localized to the cytoplasm or nucleus (Fig. 5F). Conversely, Flag-Nwd1-C, which only contains the WD40 repeat domain, was explicitly localized to the ER (Fig. 5F), indicating that the C-terminal WD40 repeat domain of Nwd1 is crucial for its ER localization and thus for interactions with ER proteins. Generally, the WD peptide motif folds into a β-propeller structure, and proteins containing WD40 repeats are believed to serve as platforms for assembling protein complexes or as mediators of transient interactions between other proteins[52]. Similarly, the predominant ER localization of Nwd1 was demonstrated in cultured AML12 cells (Supplementary Fig. 6).

Among the ER proteins identified as potential Nwd1-binding proteins, we focused on SERCA2b, which had the highest spectral count in the pulldown assay (Fig. 5B). SERCA2 is an ATPase pump embedded to the ER membrane that transports Ca^{2+} from the cytosol to the ER lumen at the expense of ATP hydrolysis[16]. Immunostaining revealed that the intracellular distribution of Nwd1 protein was identical to that of endogenous and exogenous SERCA2 protein (Fig. 5H, I). The protein topology of SERCA2b includes a cytoplasmic region comprising an actuator (A) domain (amino acids 1–43 and 124–235), a nucleotide-binding (N) domain (amino acids 360–600), a phosphorylation (P) domain (amino acids 330–359 and 601–739), and 11 transmembrane domains[53,54] (Fig. 5G). As previously described[55], we generated two deletion constructs of SERCA2b named SERCA2-N and SERCA2-C. SERCA2-N contains mainly the A, N, and P domains (amino acids 1–787), and SERCA2-C corresponds to the region containing the ER lumen and the short cytoplasmic region (amino acids 788–1044; Fig. 5G). SERCA2-N or SERCA2-C was introduced to HEK293T cells with Flag-Nwd1, and their intracellular distribution was monitored. As presented in Fig. 5I, both SERCA2 deletion mutants localized to the ER similarly as full-length SERCA2 and Flag-Nwd1.

Decreased ATPase activity of SERCA2 and smaller Ca^{2+} pools in the *Nwd1*$^{-/-}$ liver ER

How does the Nwd1–SERCA2 interaction contribute to ER stress or homeostasis? ER fractions were prepared from wild-type and *Nwd1*$^{-/-}$ livers, and SERCA2 ATPase activity, which regulates Ca^{2+} transport from the cytosol to the ER lumen, was measured. The results indicated that SERCA2 ATPase activity was significantly reduced by ~70% in the *Nwd1*$^{-/-}$ liver (wild-type, 1.0 ± 0.6; *Nwd1*$^{-/-}$, 0.3 ± 0.1; Fig. 6A). Consistent with the decrease in ATPase activity, Ca^{2+} stores in the *Nwd1*$^{-/-}$ ER were depleted by ~40% (wild-type, 1.0 ± 0.1; *Nwd1*$^{-/-}$, 0.6 ± 0.03; Fig. 6B). Contrarily, the amount of Ca^{2+} inside mitochondria did not differ between wild-type and *Nwd1*$^{-/-}$ livers (wild-type, 1.0 ± 0.3; *Nwd1*$^{-/-}$, 0.9 ± 0.2; Fig. 6C). Considering the finding that SERCA2 protein expression was drastically increased by Nwd1 deficiency (Fig. 4A, B), it was likely that the proportion of SERCA2 lacking pump activity is increased in *Nwd1*$^{-/-}$ livers. These results implied that Nwd1 is required for the folding or topology of SERCA2 on the ER membrane, enabling SERCA2 to acquire proper activity.

Discussion

Previous studies illustrated that ER stress contributes to hepatic steatosis by inducing the accumulation of lipid droplets[9,10]. However, the mechanism by which ER stress in the liver influences the development of hepatic steatosis is unclear. We demonstrated that Nwd1 deficiency led to decreased Ca^{2+} storage in the ER *via* the reduction of SERCA2 ATPase activity, leading to ER stress accompanied by diverse hepatic pathologies, including the accumulation of lipid droplets and ER-derived vacuoles in hepatocytes, hepatomegaly, hepatic fibrosis, caspase-1–dependent inflammatory pyroptosis, and the hypertrophy of resident Kupffer cells along with an elevated number of leukocytes in peripheral blood (Fig. 6D). Many of the pathologies in *Nwd1*-deficient mice are comparable to those in MASH in humans. Quality control of newly synthesized proteins largely depends on the Ca^{2+} concentration in the ER lumen. For instance, the calcium-binding protein GRP78 plays a pivotal role in detecting the accumulation of misfolded proteins in the ER in cooperation with other ER transmembrane proteins

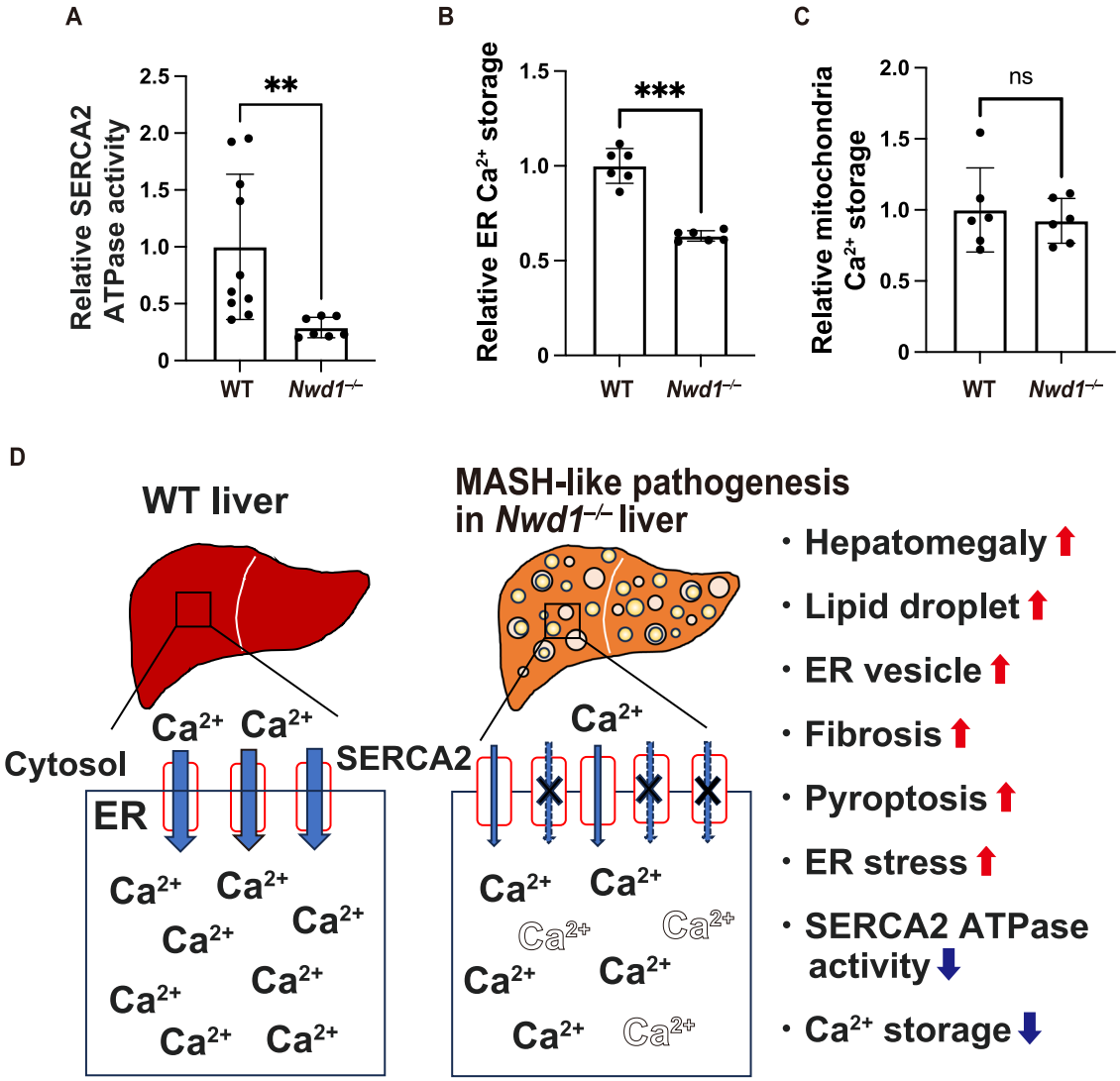

Fig. 6 | SERCA2 ATPase activity and ER Ca^{2+} storage are suppressed in the *Nwd1*$^{-/-}$ liver. A SERCA2 ATPase activity in the ER fractions of 9-month-old male wild-type ($n = 10$) and *Nwd1*$^{-/-}$ ($n = 7$) livers. Ca^{2+} storage in the ER (**B**) or mitochondrial (**C**) fractions of 3–9-month-old male wild-type and *Nwd1*$^{-/-}$ livers ($n = 6$). Welch's *t*-test, ns, not significant; **, $P < 0.01$; ***, $P < 0.001$. Black dots represent each independent biological replicate, and all graphs show the mean ± SD. **D** Summary of MASH-like hepatic pathogenesis caused by *Nwd1* deficiency and a model for dysfunction of the SERCA2 Ca^{2+} pump in the *Nwd1*$^{-/-}$ liver ER. Decreased activity of SERCA2 in the *Nwd1*$^{-/-}$ liver induces ER stress by reducing Ca^{2+} stores in the ER, leading to diverse hepatic pathologies, including the accumulation of ER-derived vacuolar structures with lipid droplets, fibrosis, and pyroptosis. The ER membranes of *Nwd1*$^{-/-}$ livers featured an increased population of SERCA2 with no or reduced pump activity (indicated by crosses and thin arrows), lowering Ca^{2+} stores inside the ER.

such as ATF6, IRE1, and PERK[56,57]. Protein disulfide isomerases, a major group of ER-resident proteins, directly interact with Ca^{2+} to serve as molecular chaperones for protein synthesis and maturation. Therefore, dysregulation of Ca^{2+} homeostasis in the ER leads to the collapse of protein quality control, resulting in the induction of ER stress[56]. It is well established that ER stress associated with unfolded proteins causes the excessive accumulation of lipid droplets surrounded by a monolayer membrane of ER-derived phospholipids in the liver[8,10,50,58–60]. On the other hand, the present qPCR analysis using whole liver tissue failed to reveal the significant upregulation of mRNA expression in major pathways associated with ER stress. As illustrated in Fig. 1, Nwd1 expression in the liver exhibited heterogeneity, with hepatocytes expressing high levels of Nwd1 being unevenly distributed, suggesting the localized ER stress in the *Nwd1*$^{-/-}$ liver that may not be detectable through qPCR analysis of the whole liver. Alternatively, the lipid accumulation observed in the *Nwd1*$^{-/-}$ liver might occur via pathways independent of ER stress. For instance, the impaired intracellular calcium dynamics, driven by altered SERCA2 activity, may affect lipid metabolic pathways by activating transcription factors such as PPARγ and SREBP-1, thereby changing the efficiency of lipid synthesis and degradation and ultimately contributing to hepatic steatosis[61,62]. It is also possible that the triggers of growth and maturation of lipid droplets might be dysregulated in the *Nwd1*$^{-/-}$ liver. Dysfunction of lipid droplet-associated proteins such as perilipins and adipose differentiation-related protein (ADRP), which play key roles in regulating lipid droplet stability and growth, might be linked to Nwd1 function[63].

Despite the abundant accumulation of lipid droplets, no significant increases in serum triglyceride and total cholesterol levels were observed in the *Nwd1*$^{-/-}$ liver. Considering that lipid droplets in the sinusoid were rarely observed in the *Nwd1*$^{-/-}$ liver using electron microscopy, along with unchanged fat levels in peripheral blood as determined by the VLDL secretion assay, this MASH-like phenotype in the *Nwd1*$^{-/-}$ liver is highly likely related to impaired hepatic fat clearance. Consistently, a previous report in mice treated with TM disclosed the induction of vacuolar structures in the liver and concomitant decreases in total cholesterol and triglyceride levels in plasma, presumably attributable to the suppression of VLDL emission from the liver[48]. Furthermore, recent studies highlighted the

involvement of pyroptosis, a caspase-1–mediated programed cell death process, in the pathology of hepatic steatosis and MASH[64]. Pyroptosis is initiated by the activation of caspase-1 through inflammasome formation, leading to pore formation in the plasma membrane and the release of pro-inflammatory factors into the pericellular space. Specifically, the release of caspase-1–dependent inflammatory complexes in hepatocytes promotes liver fibrosis and the excessive accumulation of extracellular matrix proteins, including collagen[43]. Inhibiting pyroptosis has been reported to effectively reduce fat deposition in the liver and reduce liver inflammation in MASH[65]. Along the same lines, increased pyroptosis might have driven fibrosis in the *Nwd1*$^{-/-}$ liver. Deciphering the molecular functions of Nwd1 could shed light on the aspects of the etiology of diseases associated with increased ER stress and impaired Ca^{2+} homeostasis, such as MASLD and MASH. Additionally, a recent study using RNA-sequencing data from a large cohort of MASH liver samples showed a significant reduction in *Nwd1* expression in the livers of MASH patients. Specifically, *Nwd1* mRNA expression was reduced to ~7% (log2 fold-change of −3.77) in MASH patients with lobular inflammation and 3% (log2 fold-change of −4.81) in those with fibrosis, compared to healthy controls. This suggests that loss of function of *Nwd1* might contribute to the development of MASH in humans, as it does in mice[66]. Nevertheless, we can not exclude the possibility that Nwd1 deficiency disrupts homeostasis in tissues other than the liver, leading to secondary effects on the liver through alterations in various mediator molecules that induce inflammation or ER stress. We are currently attempting to generate and analyze a hepatocyte-specific *Nwd1*$^{-/-}$ mouse line.

Nwd1 might play an essential role as a co-chaperone in modulating the activity or conformational regulation of SERCA2 on the ER membrane by binding to a specific domain of SERCA2. Immunoelectron microscopy revealed that Nwd1 localizes on the membrane or in close proximity to the cytoplasmic side of the ER, but it was rarely found within the ER. SERCA2 consists of cytosolic ATPase domains and the C-terminal short region that plays a role in Ca^{2+} affinity. A previous study found that the topological fluctuation of SERCA2b is essential for the transition of Ca^{2+} affinity[54]. Nwd1 might affect the Ca^{2+} affinity of SERCA2 by regulating its topology through binding to the C-terminal region and modulating ATPase activity through binding to the A, N, and P domains of SERCA2. The elevated expression of SERCA2 protein observed in *Nwd1*$^{-/-}$ livers might be attributable to a compensatory mechanism in response to the increased proportion of SERCA2 lacking proper pump activity.

Our previous study illustrated that Nwd1 regulates the formation of purinosomes during cerebral cortex development by interacting with PAICS, an enzyme required for de novo purine biosynthesis[19]. The purinosome is a macromolecular metabolic complex consisting of six enzymes that catalyze de novo purine biosynthesis and chaperone proteins necessary for the association of component proteins[67]. Nwd1 is also reported to interact with several chaperones in prostate cancer cell lines[68]. These facts led us to speculate that Nwd1 might function as a co-chaperone for protein folding, allowing target proteins, including SERCA2, to acquire appropriate activity. Elucidating the molecular machinery by which *Nwd1* is involved in hepatocellular pathology could provide clues to understanding the mechanisms of MASH pathogenesis and developing therapeutic strategies for MASH associated with ER stress.

Data availability

Original blot/gel images can be found in Supplementary Information and original numerical data sets used to make graphs are available in Supplementary Data 1. Further information and requests for resources and reagents should be directed to and will be fulfilled by the lead contact, Shinichi Sakakibara (E-mail: sakakiba@waseda.jp).

Received: 19 February 2024; Accepted: 11 February 2025;
Published online: 11 March 2025

References

1. Rinella, M. E. et al. A multisociety Delphi consensus statement on new fatty liver disease nomenclature. *Hepatology* **78**, 1966–1986 (2023).
2. Friedman, S. L., Neuschwander-Tetri, B. A., Rinella, M. & Sanyal, A. J. Mechanisms of NAFLD development and therapeutic strategies. *Nat. Med.* **24**, 908–922 (2018).
3. Gluchowski, N. L., Becuwe, M., Walther, T. C. & Farese, R. V. Jr. Lipid droplets and liver disease: from basic biology to clinical implications. *Nat. Rev. Gastroenterol. Hepatol.* **14**, 343–355 (2017).
4. Scorletti, E. & Carr, R. M. A new perspective on NAFLD: focusing on lipid droplets. *J. Hepatol.* **76**, 934–945 (2022).
5. Ben-Moshe, S. et al. Spatial sorting enables comprehensive characterization of liver zonation. *Nat. Metab.* **1**, 899–911 (2019).
6. Planas-Paz, L. et al. The RSPO–LGR4/5–ZNRF3/RNF43 module controls liver zonation and size. *Nat. Cell Biol.* **18**, 467–479 (2016).
7. Birchmeier, W. Orchestrating Wnt signalling for metabolic liver zonation. *Nat. Cell Biol.* **18**, 463–465 (2016).
8. Gonzalez-Rodriguez, A. et al. Impaired autophagic flux is associated with increased endoplasmic reticulum stress during the development of NAFLD. *Cell Death Dis.* **5**, e1179 (2014).
9. Flessa, C. M. et al. Endoplasmic reticulum stress and autophagy in the pathogenesis of non-alcoholic fatty liver disease (NAFLD): current evidence and perspectives. *Curr. Obes. Rep.* **10**, 134–161 (2021).
10. Ajoolabady, A. et al. Endoplasmic reticulum stress in liver diseases. *Hepatology* **77**, 619–639 (2023).
11. Malhi, H. & Kaufman, R. J. Endoplasmic reticulum stress in liver disease. *J. Hepatol.* **54**, 795–809 (2011).
12. Salo, V. T. et al. Seipin regulates ER–lipid droplet contacts and cargo delivery. *EMBO J.* **35**, 2699–2716 (2016).
13. Ali, E. S., Rychkov, G. Y. & Barritt, G. J. Deranged hepatocyte intracellular Ca^{2+} homeostasis and the progression of non-alcoholic fatty liver disease to hepatocellular carcinoma. *Cell Calcium* **82**, 102057 (2019).
14. Chen, C. C. et al. Emerging roles of calcium signaling in the development of non-alcoholic fatty liver disease. *Int. J. Mol. Sci.* **23**, 256 (2021).
15. Khamphaya, T. et al. Nonalcoholic fatty liver disease impairs expression of the type II inositol 1,4,5-trisphosphate receptor. *Hepatology* **67**, 560–574 (2018).
16. Zhao, Y. G. et al. The ER-localized transmembrane protein EPG-3/VMP1 regulates SERCA activity to control ER-isolation membrane contacts for autophagosome formation. *Mol. Cell* **67**, 974–989 (2017).
17. Park, S. W., Zhou, Y., Lee, J., Lee, J. & Ozcan, U. Sarco (endo) plasmic reticulum Ca^{2+}-ATPase 2b is a major regulator of endoplasmic reticulum stress and glucose homeostasis in obesity. *Proc. Natl Acad. Sci. USA* **107**, 19320–19325 (2010).
18. Yamada, S. & Sakakibara, S. Expression profile of the STAND protein Nwd1 in the developing and mature mouse central nervous system. *J. Comp. Neurol.* **526**, 2099–2114 (2018).
19. Yamada, S., Sato, A. & Sakakibara, S. Nwd1 regulates neuronal differentiation and migration through purinosome formation in the developing cerebral cortex. *iScience* **23**, 101058 (2020).
20. Leipe, D. D., Koonin, E. V. & Aravind, L. STAND, a class of P-loop NTPases including animal and plant regulators of programmed cell death: multiple, complex domain architectures, unusual phyletic patterns, and evolution by horizontal gene transfer. *J. Mol. Biol.* **343**, 1–28 (2004).
21. Yamada, S., Furukawa, R. & Sakakibara, S. Identification and expression profile of novel STAND gene Nwd2 in the mouse central nervous system. *Gene Expr. Patterns* **46**, 119284 (2022).
22. Horii, T., Kobayashi, R. & Hatada, I. Generation of floxed mice by sequential electroporation. In *Genome Editing in Animals: Methods and Protocols* Vol. 2637, 135–147 (Springer, 2023).
23. Matsumura, H., Hasuwa, H., Inoue, N., Ikawa, M. & Okabe, M. Lineage-specific cell disruption in living mice by Cre-mediated

expression of diphtheria toxin A chain. *Biochem. Biophys. Res. Commun.* **321**, 275–279 (2004).
24. Stielow, B., Finkernagel, F., Stiewe, T., Nist, A. & Suske, G. MGA, L3MBTL2 and E2F6 determine genomic binding of the non-canonical Polycomb repressive complex PRC1.6. *PLoS Genet.* **14**, e1007193 (2018).
25. Sanjabi, S. et al. A c-Rel subdomain responsible for enhanced DNA-binding affinity and selective gene activation. *Genes Dev.* **19**, 2138–2151 (2005).
26. Lytton, J. & MacLennan, D. Molecular cloning of cDNAs from human kidney coding for two alternatively spliced products of the cardiac Ca^{2+}-ATPase gene. *J. Biol. Chem.* **263**, 15024–15031 (1988).
27. Ma, W. & Mayr, C. A membraneless organelle associated with the endoplasmic reticulum enables 3′ UTR-mediated protein-protein interactions. *Cell* **175**, 1492–1506 (2018).
28. Hasegawa, Y., Yoshida, D., Nakamura, Y. & Sakakibara, S. Spatiotemporal distribution of SUMOylation components during mouse brain development. *J. Comp. Neurol.* **522**, 3020–3036 (2014).
29. Folch, J., Lees, M. & Stanley, G. S. A simple method for the isolation and purification of total lipids from animal tissues. *J. Biol. Chem.* **226**, 497–509 (1957).
30. Imai, N. et al. Hepatocyte-specific depletion of UBXD8 induces periportal steatosis in mice fed a high-fat diet. *PLoS ONE* **10**, e0127114 (2015).
31. Adachi, Y. et al. Drp1 tubulates the ER in a GTPase-independent manner. *Mol. Cell* **80**, 621–632 (2020).
32. Wieckowski, M. R., Giorgi, C., Lebiedzinska, M., Duszynski, J. & Pinton, P. Isolation of mitochondria-associated membranes and mitochondria from animal tissues and cells. *Nat. Protoc.* **4**, 1582–1590 (2009).
33. Yamada, S., Sato, A., Ishihara, N., Akiyama, H. & Sakakibara, S. Drp1 SUMO/deSUMOylation by Senp5 isoforms influences ER tubulation and mitochondrial dynamics to regulate brain development. *iScience* **24**, 103484 (2021).
34. Na, Y. et al. Runx1/3-driven adaptive endoplasmic reticulum stress pathways contribute to neurofibromagenesis. *Oncogene* **42**, 1038–1047 (2023).
35. Wang, X., Spandidos, A., Wang, H. & Seed, B. PrimerBank: a PCR primer database for quantitative gene expression analysis, 2012 update. *Nucleic Acids Res.* **40**, D1144–D1149 (2012).
36. Sicari, D., Delaunay-Moisan, A., Combettes, L., Chevet, E. & Igbaria, A. A guide to assessing endoplasmic reticulum homeostasis and stress in mammalian systems. *FEBS J.* **287**, 27–42 (2020).
37. Shi, J. et al. The PERK/PKR-eIF2α pathway negatively regulates porcine hemagglutinating encephalomyelitis virus replication by attenuating global protein translation and facilitating stress granule formation. *J. Virol.* **96**, e01695–01621 (2022).
38. Matsubara, T. et al. Metabolomics identifies an inflammatory cascade involved in dioxin- and diet-induced steatohepatitis. *Cell Metab.* **16**, 634–644 (2012).
39. Huang, D. W. et al. DAVID bioinformatics resources: expanded annotation database and novel algorithms to better extract biology from large gene lists. *Nucleic Acids Res.* **35**, W169–W175 (2007).
40. Huang, D. W., Sherman, B. T. & Lempicki, R. A. Systematic and integrative analysis of large gene lists using DAVID bioinformatics resources. *Nat. Protoc.* **4**, 44–57 (2009).
41. Kanehisa, M. & Goto, S. KEGG: kyoto encyclopedia of genes and genomes. *Nucleic Acids Res.* **28**, 27–30 (2000).
42. Kraupp, B. G. et al. In situ detection of fragmented DNA (TUNEL assay) fails to discriminate among apoptosis, necrosis, and autolytic cell death: a cautionary note. *Hepatology* **21**, 1465–1468 (1995).
43. Gaul, S. et al. Hepatocyte pyroptosis and release of inflammasome particles induce stellate cell activation and liver fibrosis. *J. Hepatol.* **74**, 156–167 (2021).
44. Bergsbaken, T., Fink, S. L. & Cookson, B. T. Pyroptosis: host cell death and inflammation. *Nat. Rev. Microbiol.* **7**, 99–109 (2009).
45. Li, D. et al. The ER-localized protein DFCP1 modulates ER-lipid droplet contact formation. *Cell Rep.* **27**, 343–358 (2019).
46. Combot, Y. et al. Seipin localizes at endoplasmic-reticulum-mitochondria contact sites to control mitochondrial calcium import and metabolism in adipocytes. *Cell Rep.* **38**, 110213 (2022).
47. Mashek, D. G. Hepatic lipid droplets: a balancing act between energy storage and metabolic dysfunction in NAFLD. *Mol. Metab.* **50**, 101115 (2021).
48. Yamamoto, K. et al. Induction of liver steatosis and lipid droplet formation in ATF6α-knockout mice burdened with pharmacological endoplasmic reticulum stress. *Mol. Biol. Cell* **21**, 2975–2986 (2010).
49. Lee, A. S. The ER chaperone and signaling regulator GRP78/BiP as a monitor of endoplasmic reticulum stress. *Methods* **35**, 373–381 (2005).
50. Zhu, G. & Lee, A. S. Role of the unfolded protein response, GRP78 and GRP94 in organ homeostasis. *J. Cell. Physiol.* **230**, 1413–1420 (2015).
51. Chen, X., Shi, C., He, M., Xiong, S. & Xia, X. Endoplasmic reticulum stress: molecular mechanism and therapeutic targets. *Signal Transduct. Target. Ther.* **8**, 352 (2023).
52. Jain, B. P. & Pandey, S. WD40 repeat proteins: signalling scaffold with diverse functions. *Protein J.* **37**, 391–406 (2018).
53. Chen, B., Mahaney, J. E., Mayer, M. U., Bigelow, D. J. & Squier, T. C. Concerted but noncooperative activation of nucleotide and actuator domains of the Ca-ATPase upon calcium binding. *Biochemistry* **47**, 12448–12456 (2008).
54. Zhang, Y. et al. Cryo-EM structures of SERCA2b reveal the mechanism of regulation by the luminal extension tail. *Sci. Adv.* **6**, eabb0147 (2020).
55. Kim, H. et al. Tmem64 modulates calcium signaling during RANKL-mediated osteoclast differentiation. *Cell Metab.* **17**, 249–260 (2013).
56. Krebs, J., Agellon, L. B. & Michalak, M. Ca^{2+} homeostasis and endoplasmic reticulum (ER) stress: An integrated view of calcium signaling. *Biochem. Biophys. Res. Commun.* **460**, 114–121 (2015).
57. Malhotra, J. D. & Kaufman, R. J. The endoplasmic reticulum and the unfolded protein response. *Semin. Cell Dev. Biol.* **18**, 716–731 (2007).
58. Lebeaupin, C. et al. Endoplasmic reticulum stress signalling and the pathogenesis of non-alcoholic fatty liver disease. *J. Hepatol.* **69**, 927–947 (2018).
59. Martin, S. & Parton, R. G. Lipid droplets: a unified view of a dynamic organelle. *Nat. Rev. Mol. Cell Biol.* **7**, 373–378 (2006).
60. Tauchi-Sato, K., Ozeki, S., Houjou, T., Taguchi, R. & Fujimoto, T. The surface of lipid droplets is a phospholipid monolayer with a unique fatty acid composition. *J. Biol. Chem.* **277**, 44507–44512 (2002).
61. Wang, Y., Nakajima, T., Gonzalez, F. J. & Tanaka, N. PPARs as metabolic regulators in the liver: lessons from liver-specific PPAR-null mice. *Int. J. Mol. Sci.* **21**, 2061 (2020).
62. Seebacher, F., Zeigerer, A., Kory, N. & Krahmer, N. Hepatic lipid droplet homeostasis and fatty liver disease. *Semin. Cell Dev. Biol.* **108**, 72–81 (2020).
63. Motomura, W. et al. Up-regulation of ADRP in fatty liver in human and liver steatosis in mice fed with high fat diet. *Biochem. Biophys. Res. Commun.* **340**, 1111–1118 (2006).
64. Beier, J. I. & Banales, J. M. Pyroptosis: an inflammatory link between NAFLD and NASH with potential therapeutic implications. *J. Hepatol.* **68**, 643–645 (2018).
65. Mridha, A. R. et al. NLRP3 inflammasome blockade reduces liver inflammation and fibrosis in experimental NASH in mice. *J. Hepatol.* **66**, 1037–1046 (2017).
66. Gerhard, G. S. et al. Transcriptomic profiling of obesity-related nonalcoholic steatohepatitis reveals a core set of fibrosis-specific genes. *J. Endocr. Soc.* **2**, 710–726 (2018).
67. French, J. B. et al. Spatial colocalization and functional link of purinosomes with mitochondria. *Science* **351**, 733–737 (2016).

68. Correa, R. G., Krajewska, M., Ware, C. F., Gerlic, M. & Reed, J. C. The NLR-related protein NWD1 is associated with prostate cancer and modulates androgen receptor signaling. *Oncotarget* **5**, 1666 (2014).

Acknowledgements

This work was funded by the Japan Society for the Promotion of Science grants-in-aid (KAKENHI) grant numbers 23K05996 (to S.S.) and 21K20701 (to S.Y.), the Research Support Project for Life Science and Drug Discovery (Basis for Supporting Innovative Drug Discovery and Life Science Research) from AMED under Grant Number JP21am0101120 (to I.H.), Gout and Uric Acid Research Foundation 2020 (to S.S.) and 2022 (to S.Y.), and Waseda University Grants for Special Research Projects 2021C-611 (to S.Y.), 2022C-611 (to S.Y.), 2022C-214 (to S.S.), and 2023C-207 (to S.S.). We would like to thank Ms. M. Mori and Ms. M. Hidaka for their technical assistance. We also thank Enago (www.enago.jp) for English editing.

Author contributions

Study concept and design: S.Y. and S.S. Acquisition of data: S.Y., H.O., M.F., M.K., K.N., T.M., K.K., T.H., R.K., I.H., and S.S. Analysis and interpretation of data: S.Y., K.N., and S.S. Drafting of the manuscript: S.Y., T.H., and S.S. Obtained funding: S.Y., I.H., and S.S.

Competing interests

The authors declare no competing interests.

Additional information

Supplementary information The online version contains supplementary material available at https://doi.org/10.1038/s42003-025-07717-5.

Correspondence and requests for materials should be addressed to Seiya Yamada or Shin-ichi Sakakibara.

Peer review information *Communications Biology* thanks Zhao-Qing Shen and the other, anonymous, reviewer(s) for their contribution to the peer review of this work. Primary Handling Editors: Joao Valente.